Doc. #: GC-131211.a

G-CLEF Science Requirements

Prepared By:

Anna Frebel – G-CLEF Science Working Group Chair

Andrew Szentgyorgyi – G-CLEF Principal Investigator

27 Jan 2014

Prepared By	Title	Date
Anna Frebel	Chair, SWG	11 Dec 2013
Andrew Szentgyorgyi	PI	11 Dec 2013
Approved By	**Title**	**Date**

Revision History

Issue	Date	Changes	Authors
Draft	11 Dec 2013	————————	AF & ASz
SRR Rel.	11 Dec 2013	For SRR Review	ASz
Rev.1	27 Jan 2014	Incorporate SRR input	

Table of Contents

Table of Figures

Table of Tables

Acronym Dictionary

AIT	Assembly Integration Test	MANIFEST	Many Instrument Fiber System
AOTS	Adapted Off-The-Shelf	PDR	Preliminary Design Review
CoDR	Concept Design Review	PDS	Preliminary Design Study
CCD	Charge Coupled Device	OCIW	Observatories of the Carnegie Institution of Washington
Cheops	Characterizing ExOPlanets Satellite	PA	Precision Abundance
CoDS	Concept Design Study	PI	Principal Investigator
CWL	Center Wavelength	PRV	Precision Radial Velocity
FOV	Field of View	PRVS	Precision Radial Velocity Spectrograph
FWHM	Full Width, Half Maximum	SAO	Smithsonian Astrophysical Obs
G-CLEF	GMT-Consortium Large Earth Finder	SDSS-III	Sloan Digital Sky Survey-III
GMT	Giant Magellan Telescope	SNe	Supernovae
GMTO	Giant Magellan Telescope Organization	SWG	Science Working Group
GRB	Gamma Ray Burst	TBC	To Be Confirmed
HARPS	High Accuracy Radial velocity Planet Searcher	TBD	To Be Determined
HCO	Harvard College Observatory	TBR	To Be Resolved
HU	Harvard University	TESS	Transiting Exoplanet Survey Satellite
KASI	Korean Astronomy and Space Science Institute	TMT	Thirty Meter Telescope
LCO	Las Campanas Observatory	UoC	University of Chicago

Applicable Documents

GMT Science Requirements. A.1 M. Johns, P. Mc Carthy and R. Kron, GMT-SCI-REQ-00001 09/13/2013

GMT Operations Concept, Rev. 10, P. McCarthy, GMT-SCI-DOC-00034, 09/12/2013

GMT Facility Instrument Systems Engineering Plan, D. Sawyer and G. Jacoby GMT Doc #: GMT-SE-DOC-00656, Rev 1, 11/20/2013

Reference Documents

A Design Study for the GMT-CfA Large Earth Finder (G-CLEF), G-CLEF Doc #: GC-110908.a, 8 Sept 2011

The Science Case for G-CLEF, G-CLEF Doc #: GC-13111.a, 11 Nov 2013

Giant Magellan Telescope Science Requirements, Doc. # GMT-1405, 10 July 2006

1. Introduction

In this document we select several investigations from the Concept Design Review (CoDR) document - *The Science Case for G-CLEF,* henceforth referred to as the Science Case – and use them as a framework within which to develop a flowdown from Science Drivers (Level 0 Requirements) to G-CLEF Science Requirements (Level 1 Requirements). In some instances a single science objective is used to develop requirements. In these cases, an observationally demanding Science Objective which defines the outermost performance envelope of G-CLEF has been chosen.

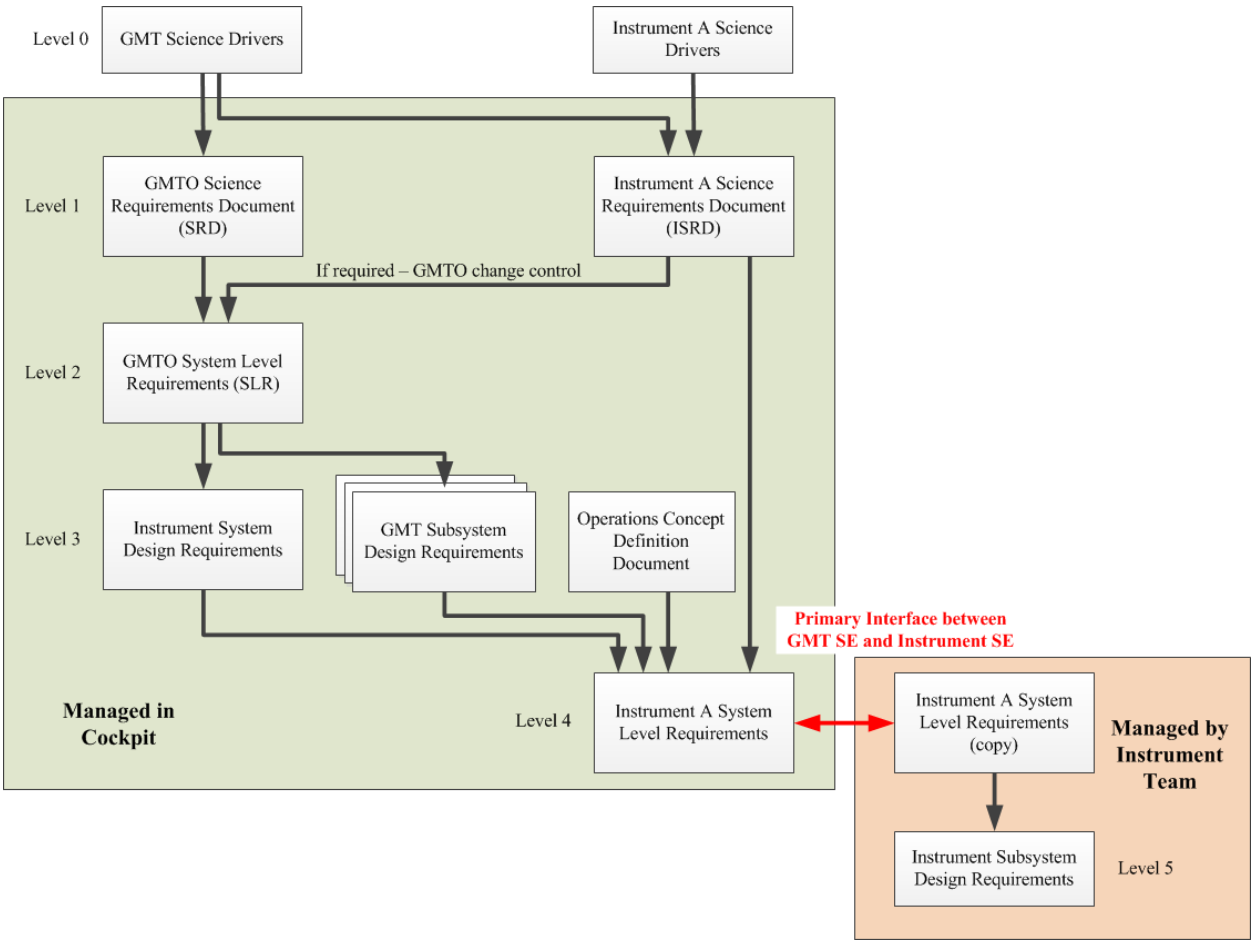

Figure 1-1. Flow down development of facility instrument requirements documents and configuration management responsibilities (from GMT-SE-DOC-00656, Rev 1.).

The flow of requirements below Level 1 for G-CLEF is diagrammed in Figure 1-1. G-CLEF Science requirements, as well as relevant GMT Level 3 Requirements are flowed to G-CLEF Systems Level Requirements at Level 4.

The programs described in this document are, for the most part, drawn G-CLEF Science Case, however the Science Case is over two years old, so the programs have been updated to the present state of the art. In some cases, new, high priority science opportunities have emerged, especially the search for biomarkers in exoplanetary atmospheres, and these have been added to the list of science drivers. The programs we choose to fiducialize the performance envelope of G-CLEF are:

- Exoplanet Science
  - Precision Radial Velocity Studies
  - Exoplanet Atmospheric Science
- Stellar Abundance Science
  - The Discovery and Characterization of the Most Metal Poor Stars
  - Abundance Around and Beyond the Local Group
- Cosmology
  - Characterizing the First Stars and the Primordial ISM
  - Searching for Variations of Fundamental Constants on Cosmological Scales

A consolidated listing of requirements is presented in the last section of this document (Section 5.1) and this matrix provides the Level 3 requirements for G-CLEF (Table 5-1).

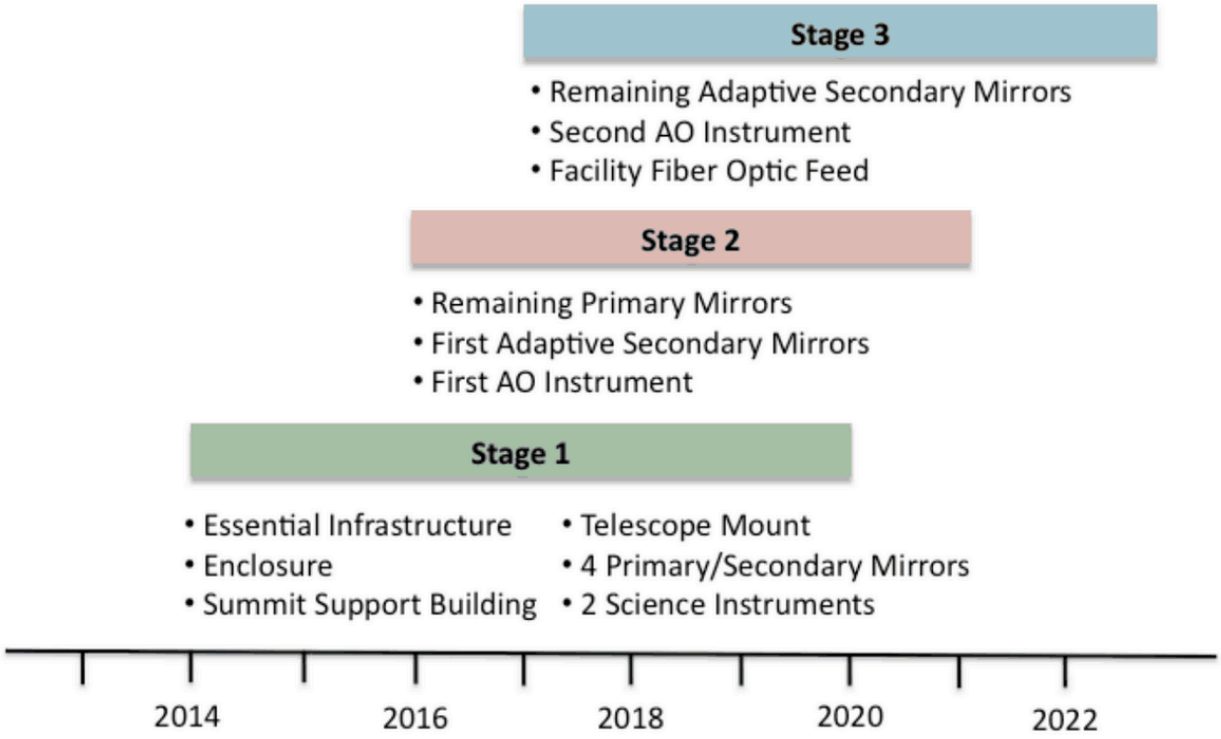

Figure 1-2: The GMT telescope phased commissioning plan.

An important issue for developing requirements is the evolutionary nature of the capabilities of the GMT itself. The phasing of the GMT capabilities is shown in Figure 1-2. First light with 4 fast steering mirrors will be August 2019. Fast steering mirror will provide some atmospheric tip-tilt and wind shake correction. The full complement of 7 primaries with 7 adaptive secondaries will be complete January 2023. The exact nature of transition from 4 to 7 mirrors and fast steering secondaries to adaptive secondaries will depend somewhat on overall progress to commissioning and the project funding profile.

Nonetheless it is essential that we ultimately demonstrate the scientific vitality of G-CLEF at each evolutionary level of the GMT in our Level 4 requirements document, specifically with:

- A four mirror telescope with fast steering secondaries
- A seven mirror telescope with fast steering secondaries
- A seven mirror telescope with adaptive secondaries.

In each science case, it is our expectation that at the earliest operational phase, observers will focus on the "low hanging fruit" – the brightest, easiest objects. As telescope capability improves, more challenging observing targets will become accessible. In most science cases discussed in this document, we describe this evolution.

2. Exoplanet Science

2.1. Precision Radial Velocity Studies of Exoplanetary Systems - Mining the TESS Catalog

2.1.1. Science Drivers (Level 0 Requirements)

Precision radial velocity (PRV) measurements of transiting exoplanets achieve three objectives – measure planetary mass, determine the eccentricity of planetary orbits and reveal the presence of non-transiting planets. This lattermost objective can, in some cases be determined from photometric data alone by measuring transit timing variations (TTVs). Transiting planets are particularly rich scientific targets because the geometry of the transit lifts the degeneracy in i·Sin (θ). Since the transit data measures the exoplanet diameter and the reflex velocity of the host star gives the exoplanet mass, it is possible to determine the exoplanetary density and hence to deduce the internal constitution of the exoplanet.

The broad science objectives of PRV studies of exoplanetary systems with G-CLEF are:

- Confirm and measure the mass of the smallest exoplanet candidates discovered in current and future transit searches, especially those in habitable zones where the planetary surface temperature supports water in liquid phase.
    - Detect radial velocity signature of Earth mass planet orbiting a Solar type star in the habitable zone (mass determination).
    - Detect radial velocity signature of Earth mass planet orbiting a low mass (M) star in the habitable zone (mass determination).
- Determine the architecture and internal dynamics of other exoplanetary systems (mass & eccentricity determination, presence of non-transiting components).
- Determine the bulk properties and internal structure of exoplanets (mass determination).
- Constrain planet migration histories (mass & eccentricity determination, presence of non-transiting components).
- Understand the uniqueness or ubiquity of the architecture of our Solar system (mass & eccentricity determination, presence of non-transiting components).

Here we develop these science drives in the context of synergistic observations with the Transiting Exoplanet Survey Satellite (TESS).

2.1.1.1. Introduction

TESS is an all-sky, photometric survey instrument that will search for the nearest, and therefore brightest, transiting exoplanet candidates. It has been selected for launch by NASA in early 2018. Characterizing ExOPlanet Satellite (CHEOPS) will be a pointed mission that will do extremely precise photometry on transiting systems on a one-at-a-time basis and will focus on planets in the 1 – 6 R_{Earth} range. CHEOPS has been selected for launch by ESA as an S-class mission. It is scheduled for launch in 2017. Both instruments will start producing useful data approximately 1 year before G-CLEF first light. Since CHEOPS will not observe the whole sky, its capability for observing long period Earth twins orbiting G stars in the habitable zone may be better that that of TESS, depending somewhat on the science focus the mission team chooses. However the science rationale for CHEOPS is evolving and it is not clear what the balance between discovery and follow up observations will be. TESS is expected to find numerous bright transiting exoplanetary systems, some of which will have rocky planets in the habitable zone of solar-type stars. For this reason we focus on the TESS – G-CLEF synergy. We note the TESS Science Center will be a joint MIT-CfA initiative.

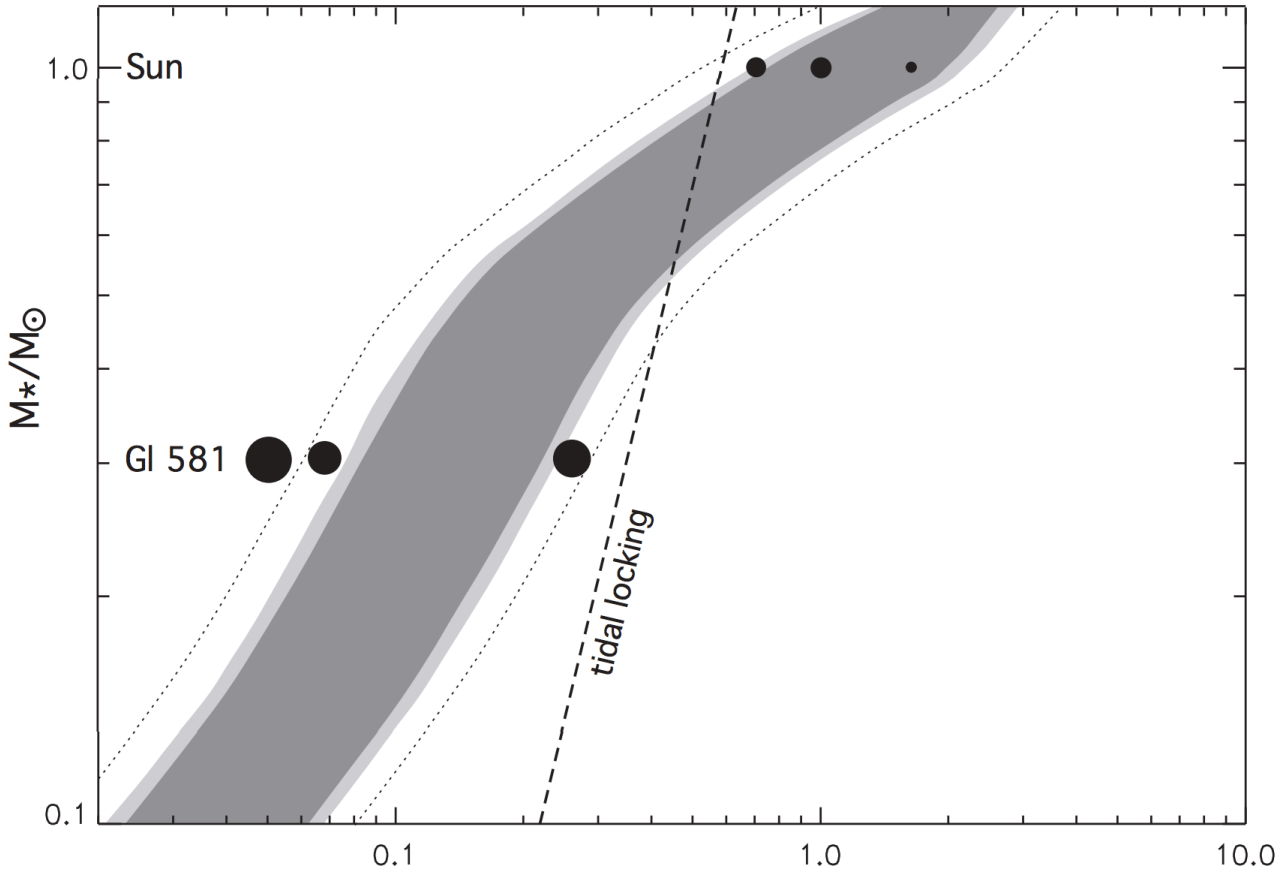

Figure 2-1: The theoretical continuous (> 5 Gyr) habitable zone as a function of stellar mass (shaded region). The different shading areas correspond to various assumptions on cloudiness and the efficiency of the runaway greenhouse. The dotted lines delineate the extreme outer edges of the habitable zone. Planets inward of the dashed line become tidally locked in less than 1 Gyr. The loci of Venus, Earth, and Mars are plotted. The orbital positions and relative sizes of the first three planets discovered orbiting the M dwarf GJ 581 (Udry et al. 2007) are also shown. The corresponding orbital periods of habitable-zone planets around stars with masses between 0.1 and 0.2 $M_{\odot}$ are between approximately 4.5 and 70 d. These planets have small orbital radii, so they have a high probability of transiting and would be excellent targets for atmospheric studies with upcoming facilities like JWST and G-CLEF. Figure from Selsis et al. 2007.

2.1.1.2. The TESS Discovery Space

The most important contribution TESS will make to exoplanet science will be to provide us with a large catalog of exoplanets orbiting bright stars. The most important results in exoplanet research are based on observations of a very small number of bright stars known to have transiting planets. While the Kepler mission has so far made approximately 3000 new exoplanet candidate discoveries, they

are relatively faint (M_R ~10-16). For this reason, detailed studies of Kepler Objects of Interest (KOIs) are only possible for a few of the very brightest Kepler exoplanet candidates. This is illustrated by Figure 2-2, where we compare the yield of Kepler & ground based transit surveys to the predicted yield from TESS. While ground based surveys have discovered a number of very bright exoplanet systems, their yield is low. Kepler has discovered only one KOI with a host star brightness approaching 8th magnitude. TESS on the other hand, is expected to yield numerous systems in the 4th to 13th magnitude band. These are the systems we will observe to study atmospheres, determine planetary "geophysics", search for signatures of biomarkers and perhaps someday interrogate for evidence of extraterrestrial intelligence.

The TESS instrumentation consists of four CCD cameras, each with a field of view of 23° on a side for a total simultaneous field of view of 23° x 90° (see Figure 2-3). The lenses are F/1.6 with a 150 mm focal length - a custom design by Lincoln Laboratories. The focal plane is a mosaic of four custom CCDs (CCID - 76), also designed and fabricated by Lincoln Labs. The imaging format is 4k x 4k, 15μ pixels and is read out in frame transfer mode. Each pixel is 21 arcsec on a side. The exposure time is 2 seconds yielding a signal-to-noise (S/N) of 100 on a M_I=10 star in each exposure.

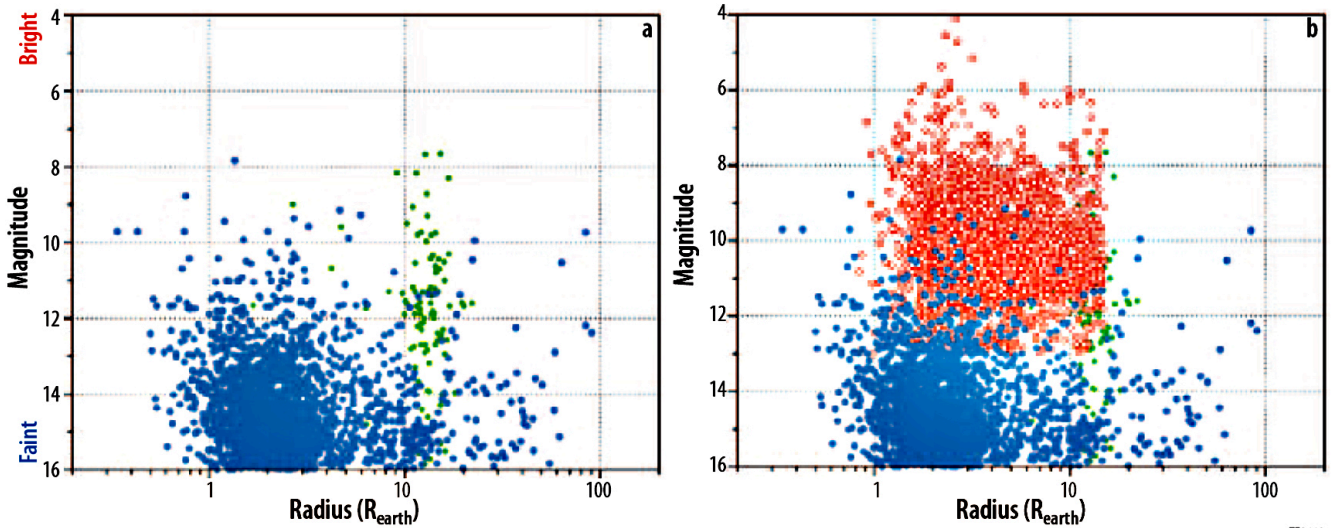

Figure 2-2: Comparison of brightness of Kepler discoveries (plotted in blue), ground-based transit surveys (in green) and the expected TESS yield (in red) - (from the TESS Concept Study Report).

The yield of exoplanetary orbital periods will depend critically on the specific exposure time on a particular region of the celestial sphere. The 23° x 90° field of view of the TESS camera divides each hemisphere into 13 swaths each of which are observed with a dwell time of 27 days. The northern hemisphere will be observed in the first year and the Southern hemisphere in the second year. A longer, extended mission is a possibility, but not a certainty. The exposure map is shown in the right panel of Figure 2-3. At low ecliptic latitude, the exposure time is 27 days, however at

higher latitude the exposure increases to a maximum 355 days near the pole. Small strips parallel to lines of latitude are missed with this survey mapping and sky coverage is ~90%. TESS is in an extremely eccentric, high Earth orbit where the apogee is outside the orbit of the Moon (see Figure 2-4). This reduces gaps in the data series drastically; the orbital period is 13.7 days, with a brief 20 hour dead time near perigee, so the observing duty cycle is very high and orbital phase coverage is nearly complete.

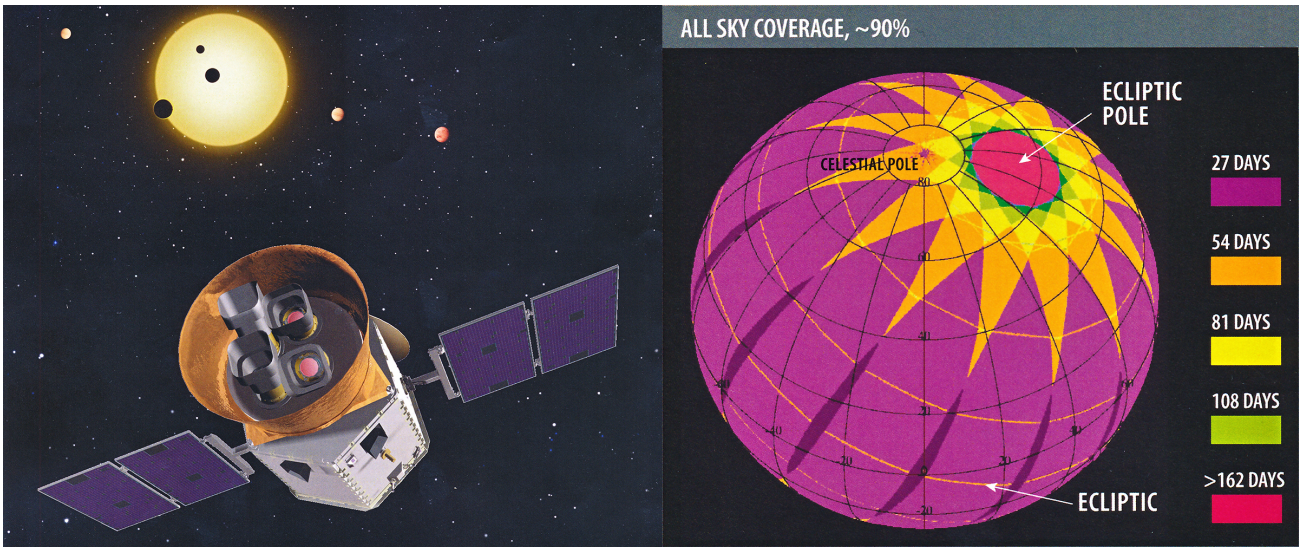

Figure 2-3: Left panel: The TESS satellite showing the 4 TESS wide-field cameras. Right panel: Sky coverage for a two year mission lifetime (from the TESS Concept Study Report.)

While the actual yield of exoplanets discovered by TESS must await the completion of the TESS mission itself, our understanding of the frequency distributions of exoplanets has sharpened quite a bit of late – see e.g Dressing, 2013 or Fressin et al. 2013. For this reason, it is possible to extrapolate from currently available catalogs to predict the nature of the systems we will discover with TESS with an ever-improving level of confidence. The total number of exoplanets discovered, the mass distribution of those planets and the spectral type of their host stars can be modeled based on existing catalogs and our experience with previous and ongoing massive photometry programs, especially Kepler.

The TESS team has an active modeling program to estimate the TESS exoplanetary yield. These estimates are constantly revised as our knowledge of the census of exoplanetary systems improves. The results presented here are drawn from the TESS Concept Study Report, which was submitted in September 2012. While an even better prediction would be possible with information we have obtained in the intervening year, these predictions provide a relatively up-to-date snapshot of what we may expect as a TESS input catalog for G-CLEF.

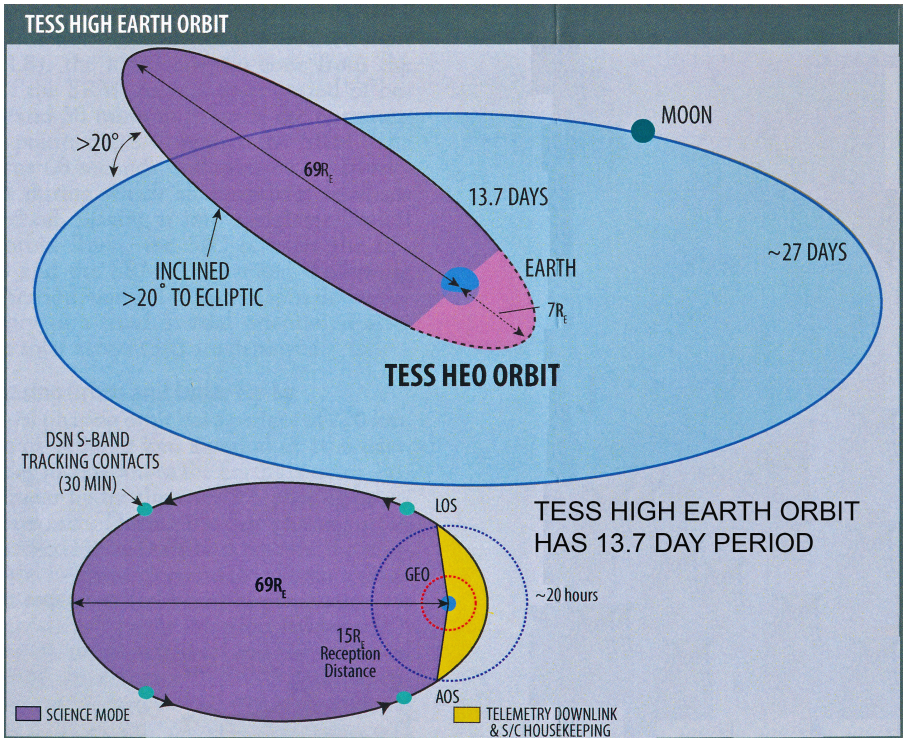

Figure 2-4: The TESS high Earth orbit has a 13.7 day period with an apogee that is slightly beyond the lunar orbit (from the TESS Concept Study Report.)

The predicted TESS yield as a function of exoplanet mass is histogrammed in Figure 2-5. The number of Earths and Super-Earth TESS is expected to discover is quite large. Not all of the orbits of the planets will be near the habitable zone, and some exoearths will be less “interesting”. Close in Earth mass planets will induce larger reflex motions in their host stars and may have their ancillary parameters measured by less capable instruments. Nonetheless, G-CLEF will be required to measure the mass and orbital eccentricity of a significant number of the most interesting and challenging of these systems.

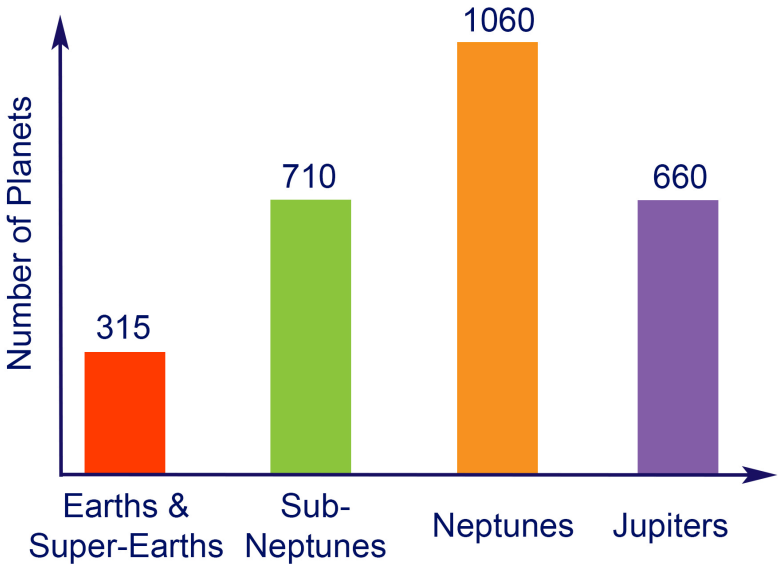

Figure 2-5: Expected TESS yield by planet/mass type (from the TESS Concept Study Report.) See Table 2-1 for classification of exoplanet by size (radius).

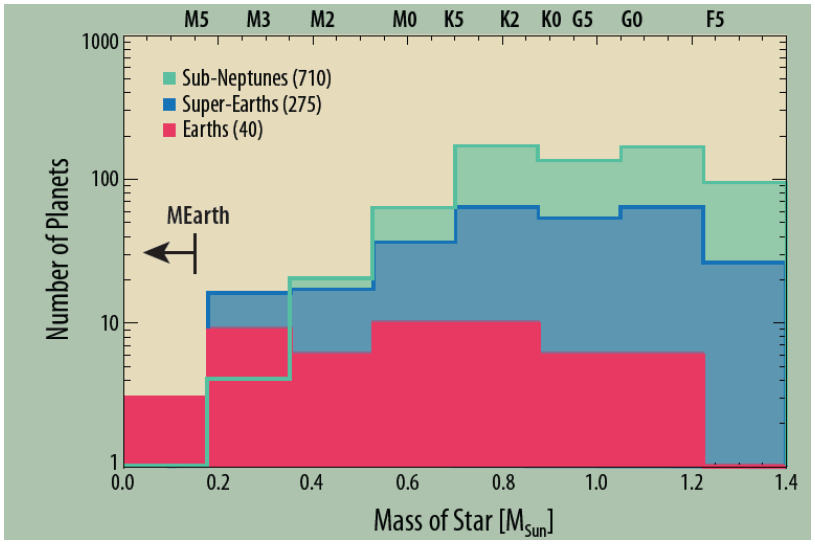

Figure 2-6: Predicted TESS yield by stellar type (from the TESS Concept Study Report.). MEarth is a ground based photometric search for exoplanets orbiting M dwarf stars.

The expected TESS yield as a function of host stellar type is presented in Figure 2-6. It can be seen that Earth-mass planets are expected to be preferentially discovered orbiting M4 to K2 stars, while the SuperEarth detections are biased towards higher mass stars. Perhaps most importantly it is to

seen that "interesting" system will be discovered around the full range of stellar types from M8 to F0.

Exoplanet Type	Radius (R_{Earth})
Earths	0.9-1.25
Super-Earths	1.25-2
Sub-Neptune	2-3
Neptune	3-6
Giant Planets (Jupiters)	6-15

Table 2-1: Exoplanet classification nomenclature by planetary radius.

The importance of G-CLEF for exoplanet science is illustrated in Figure 2-7, where a prediction of the TESS catalog is shown in a scatter plot as a function of planet radius, orbital period and number of transits detected. While short period planets will have numerous transits measured over the duration of the TESS mission, for longer period orbits, the probability of triple, double or even single transit observations for a given system decreases. The evidence for the existence of the most interesting systems, i.e. those with the longest periods, will, paradoxically be the most tenuous, and additional evidence will be required to validate their identification as exoplanetary systems. PRV measurements will be required to unambiguously confirm and characterize the real exoplanetary systems. This is a critical step that must be completed before, for instance, a TESS exoplanet candidate can be selected as a target for atmospheric study with JWST.

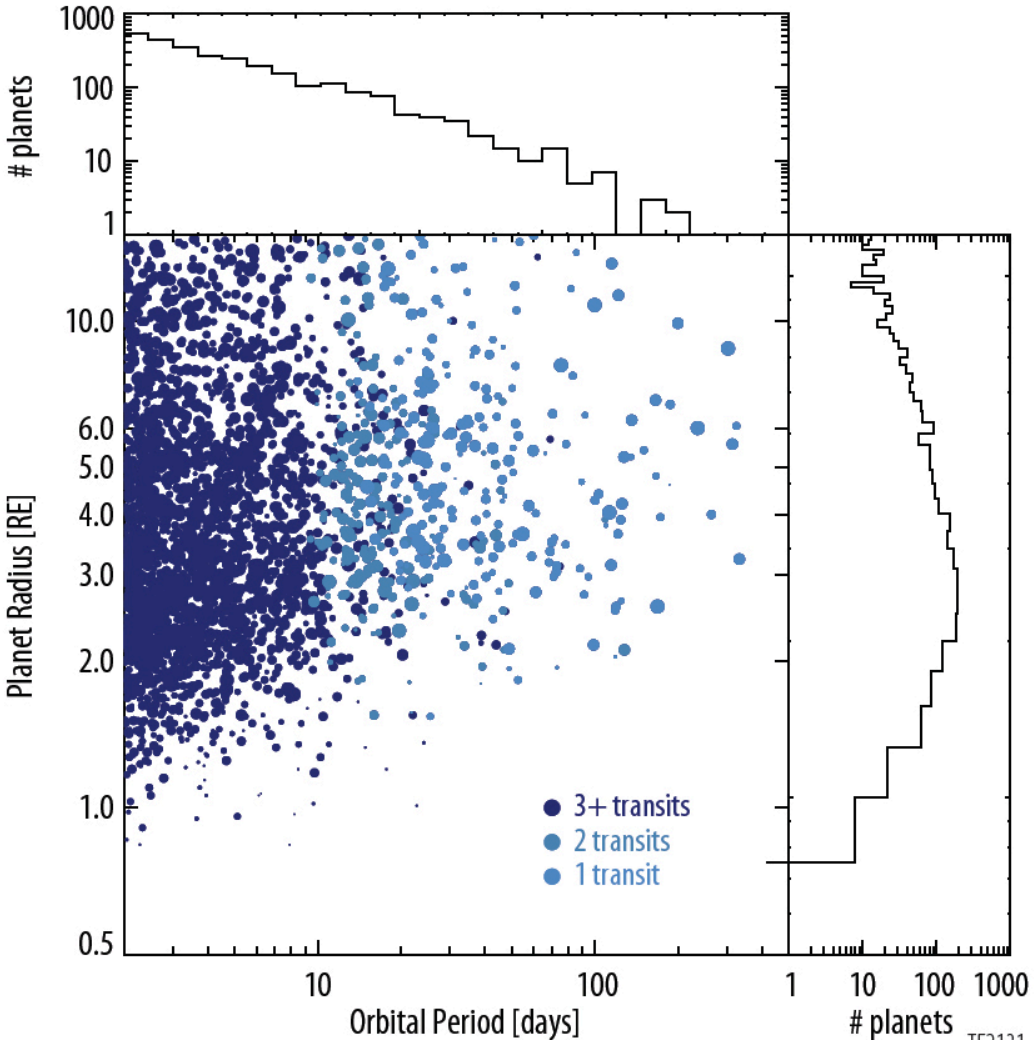

Figure 2-7: Predicted TESS exoplanet yield as a function of orbital period and planet radius (from the TESS Concept Study Report.)

2.1.2. Science Requirements (Level 1 Requirements)

To accomplish the science objectives listed in Section 2.1.1 we require that G-CLEF be capable of measuring or observing the following phenomena:

- Measure the radial velocity of a M4V star with 0.68 m/s precision over 70 day timescales for candidates, especially in the TESS catalog.
- Measure the radial velocity of a F,G or K-type star with 9 cm/sec precision over 1 year timescales, especially in the TESS catalog.

- Detect the presence of multiple planets in a single exosolar system with masses in the range of Solar system constituents.
- Determine the mass of a fair sample of exoplanets with 10% accuracy for transiting planets with 3-5% radius measurement accuracy for density determination.
- Measure stellar activity simultaneously with PRV measurement.

The primary consideration for this science mission is to optimize the radial velocity measurement precision of G-CLEF. For the range of stars from M8 to F0 stars, G-CLEF must be able to characterize exoplanets in the habitable zones of their host stars. A table of the reflex velocities of a host star in a number exoplanet/stellar type configurations is presented in

Planet	a (AU)	Reflex Velocity (K, m/sec)				
		G2V	M0V	M2V	M4V	M6V
Jupiter (318 M_{Earth})	0.1	89.8	116	136	201	284
Jupiter (318M_{Earth})	1.0	28.4	36.7	42.9	63.6	89.9
Jupiter (318 M_{Earth})	5.0	12.7	16.4	19.1	28.4	40.2
Neptune (17 M_{Earth})	0.1	4.8	6.2	7.2	10.8	15.2
Neptune (17 M_{Earth})	1.0	1.5	2.0	2.3	3.4	4.8
Super Earth (5 M_{Earth})	0.1	1.4	1.8	2.1	3.1	4.4
Super Earth (5 M_{Earth})	1.0	0.45	0.57	0.67	1.0	1.4
Earth	0.1	0.28	0.37	0.43	0.68	0.89
Earth	1.0	0.09	0.12	0.13	0.20	0.28
Mars	0.1	0.03	0.04	0.05	0.07	0.09
Mars	1.0	0.009	0.012	0.014	0.021	0.030

Table 2-2.

Planet	a (AU)	Reflex Velocity (K, m/sec)				
		G2V	M0V	M2V	M4V	M6V
Jupiter (318 M_{Earth})	0.1	89.8	116	136	201	284
Jupiter (318M_{Earth})	1.0	28.4	36.7	42.9	63.6	89.9
Jupiter (318 M_{Earth})	5.0	12.7	16.4	19.1	28.4	40.2
Neptune (17 M_{Earth})	0.1	4.8	6.2	7.2	10.8	15.2
Neptune (17 M_{Earth})	1.0	1.5	2.0	2.3	3.4	4.8
Super Earth (5 M_{Earth})	0.1	1.4	1.8	2.1	3.1	4.4
Super Earth (5 M_{Earth})	1.0	0.45	0.57	0.67	1.0	1.4
Earth	0.1	0.28	0.37	0.43	0.68	0.89
Earth	1.0	0.09	0.12	0.13	0.20	0.28
Mars	0.1	0.03	0.04	0.05	0.07	0.09
Mars	1.0	0.009	0.012	0.014	0.021	0.030

Table 2-2: Reflex velocities for a range of planets masses orbiting solar and M dwarf stars. Currently achievable radial velocity precision is coded in light beige. Extrapolation to the era of G-CLEF first light is highlighted in dark beige. G-CLEF specification precision is coded in green and goal precision is indicated in yellow.

For F, G & K dwarf stars, this implies a capability to measure the reflex motion of the host star at the 9 cm/sec level. This goal may be achieved with numerous measurements, however the number of measurements required should be consistent with the expected time that will be devoted to PRV measurements with the GMT. A simplistic calculation would suggest precision should improve as $\sqrt{N}$ where N is the number of measurements. This crude approximation ignores numerous systematics and measurement bias. While we use $\sqrt{N}$ as a proxy for a more quantitative error calculation, a more quantitative error analysis is being developed for Instrument Requirements Review (IRR), some two months hence.

In many respects, M-type dwarfs, which are lower mass than F, G & K stars, are considerably less challenging targets for the detection of Earth-mass planets in the habitable zone (

Planet	a (AU)	Reflex Velocity (K, m/sec)				
		G2V	M0V	M2V	M4V	M6V
Jupiter (318 M_{Earth})	0.1	89.8	116	136	201	284
Jupiter (318M_{Earth})	1.0	28.4	36.7	42.9	63.6	89.9
Jupiter (318 M_{Earth})	5.0	12.7	16.4	19.1	28.4	40.2
Neptune (17 M_{Earth})	0.1	4.8	6.2	7.2	10.8	15.2
Neptune (17 M_{Earth})	1.0	1.5	2.0	2.3	3.4	4.8
Super Earth (5 M_{Earth})	0.1	1.4	1.8	2.1	3.1	4.4
Super Earth (5 M_{Earth})	1.0	0.45	0.57	0.67	1.0	1.4
Earth	0.1	0.28	0.37	0.43	0.68	0.89
Earth	1.0	0.09	0.12	0.13	0.20	0.28
Mars	0.1	0.03	0.04	0.05	0.07	0.09
Mars	1.0	0.009	0.012	0.014	0.021	0.030

Table 2-2). Habitable zone orbits are smaller, the corresponding orbital period is shorter and the reflex velocity of the host star is greater. While the level of precision is within the reach of existing PRV instruments, M stars are faint, so the large aperture of the GMT is required to provide adequate S/N to study a fair sample of TESS M star candidates.

While we have set the requirement for the mass determination threshold at the mass of the Earth, it should noted that Kepler has already discovered sub-Earth diameter exoplanets, and a goal requirement for G-CLEF should be to measure the mass of a Mars-mass planet orbiting a Solar-type star (see Figure 2-8).

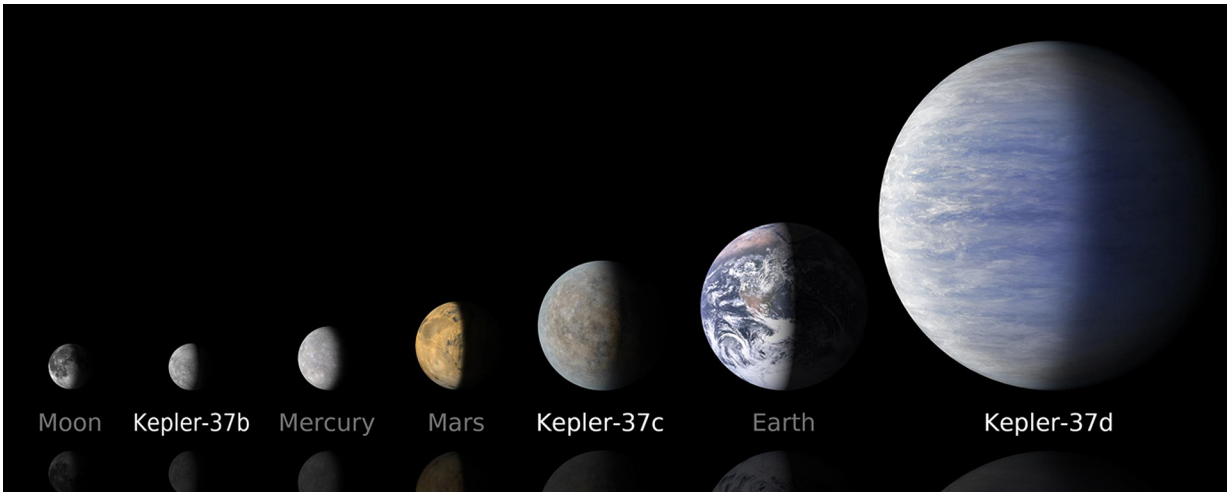

Figure 2-8: The Kepler 37 system has detected planets smaller than the Earth and almost as small as the Moon. No Northern hemisphere facility exists or is planned which can measure the mass of these exoplanets or unambiguously validate that they are exoplanets. (Credit NASA-Reuters)

To maximize the utility of G-CLEF this precision should be achievable in the shortest time possible. As we have discussed in Section 1, the capability of G-CLEF will increase as the telescope is increasingly populated with mirrors and adaptive optics comes on line. This would suggest a focus on M type stars in the early phases of telescope operations, which are less challenging targets for the detection of Earth-mass planets.

It is to be noted that all existing PRV instruments are optimized and, in some cases, limited to, observations at the blue end of the optical passband, focusing on FG & K stars. G-CLEF will observe the entire optical passband. Bean (2013) has emphasized the criticality of the 7000Å-8500Å passband for precise RV measurements of M dwarfs (see **Error! Reference source not found.**). Since it is essential to monitor stellar jitter during a PRV measurement, a capability to monitor Ca H & K line depths at 3968 & 3933Å is essential, so good response to 3900Å is required. In general, increasing bandwidth increases the number of spectral lines measured, so precision should improve as $\sqrt{N}$, if N is the total number of line in the passband.

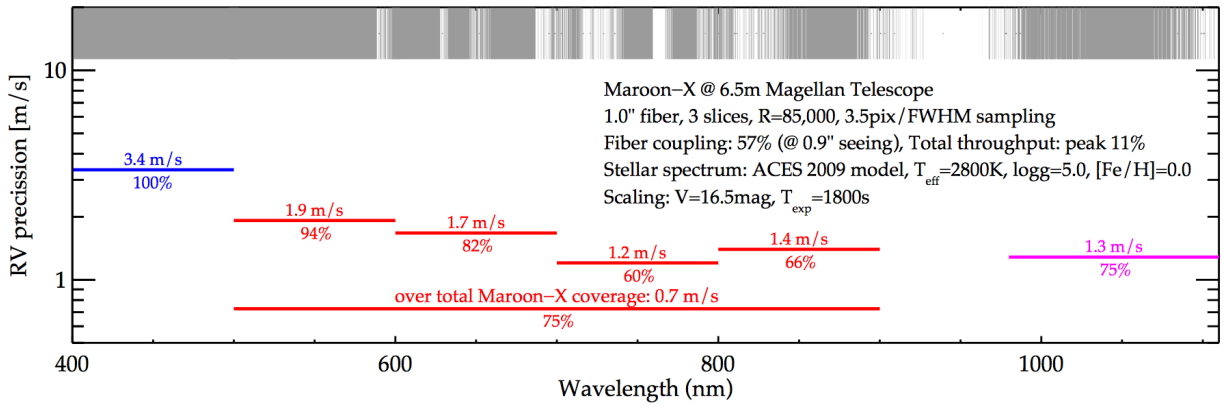

Figure 2-9: Radial velocity expected of a red-sensitive PRV spectrograph on the 6.5m Magellan telescope. The top band shows the atmospheric transmission in reverse. The achievable radial velocity for different passbands is indicated below for an M5 dwarf. It can be seen that even though there is considerable absorption in the band near 7500Å, it is the best region for PRV measurement for this star **(**Bean, 2013).

#	Requirement
2.1.1	G-CLEF shall have good sensitivity at blue wavelength so as to measure the equivalent widths of Ca H & K absorption features at 3968Å & 3933Å sufficient to use these features as a diagnostic activity stellar activity.
2.1.2	G-CLEF shall have good sensitivity in the 7000Å-9000Å to maximize radial velocity precision for M stars.
2.1.3	G-CLEF shall have good sensitivity in the 5000Å-6000Å to maximize radial velocity precision for F,G & K stars stars.
2.1.4	G-CLEF shall be able to resolve spectral features in F, G & K stars with low equatorial rotation rates and activity.
2.1.5	G-CLEF shall have long term radial velocity measurement stability sufficient to measure 10 cm/sec reflex motion of a star (4 cm/sec goal).
2.1.6	G-CLEF shall be capable of measuring the radial velocity of a large sample of stars with the cadence necessary to measure 10 cm/sec reflex motion of a star (4 cm/sec goal) with

	several day to multi-year orbital periods.

Table 2-3: G-CLEF Science Requirements (Level 1 Requirments) to enable exoplanet precision radial velocity observations.

2.1.3. References

http://cheops.unibe.ch/

Dressing, C., *2013, TESS Science Team Memo: Expected Planet Yield from a Sensitivity-Limited Target List*, TESS Technical Memorandum

Fressin, F. et al., 2013, *The False Positive Rate of Kepler and the Occurrence of Planets*, ApJ, 766 81

2.2. Exoplanet Atmospheric Science - Detecting O2 in the Atmosphere of Earth Twins

2.2.1. Science Drivers (Level 0 Requirements)

In this section we focus on requirements to detect a single biomarker molecular species (O_2) in the atmosphere of an Earth-like planet. This objective is perhaps the most challenging goal for G-CLEF envisioned in this document. However, by setting this as a requirement for G-CLEF, we guarantee capability to perform other less demanding observations of exoplanetary atmospheres.

The broader science objectives for G-CLEF in performing studies of exoplanet atmospheres are:

- Identify exoplanets with significant atmospheres
- Understand energy transport in giant exoplanet atmospheres
- Measure exoplanet atmosphere vertical temperature profiles
- Determine atomic and molecular composition of exoplanet atmospheres
- Discover biomarkers in the atmospheres of exoplanets

2.2.1.1. Introduction

The detection and characterization of exoplanet atmospheres are perhaps the most exciting, frontier areas of exoplanet research, itself a nascent subfield of astrophysics. Now that is it well established that there are numerous earth-radius planets in the nearby Universe, and we have a rudimentary understanding of the statistical distribution of exoearths and exoplanets in general (e.g. Fressin, 2013), the next frontier is to characterize planetary atmospheres – i.e. atmospheric chemical and molecular composition, particulate and haze content, heat transport & "weather" and the interplay of geophysics and atmospheric evolution. A particularly enabling development in this field is the capability to observe exoplanet atmospheres from ground-based telescopes in the presence of strong foreground telluric contamination. While the first ground-based exoplanet atmosphere observations were performed using broad-band photometric filters (Sing & Lopez-Morales 2009; de Mooij &

Snellen 2009), successul detections have now extended to precision low and high resolution spectroscopy, both in the near-IR (e.g. Bean el at. 2010, 2013; Rodler at el. 2012) and most recently in the optical passband (Jordan et al. 2013)

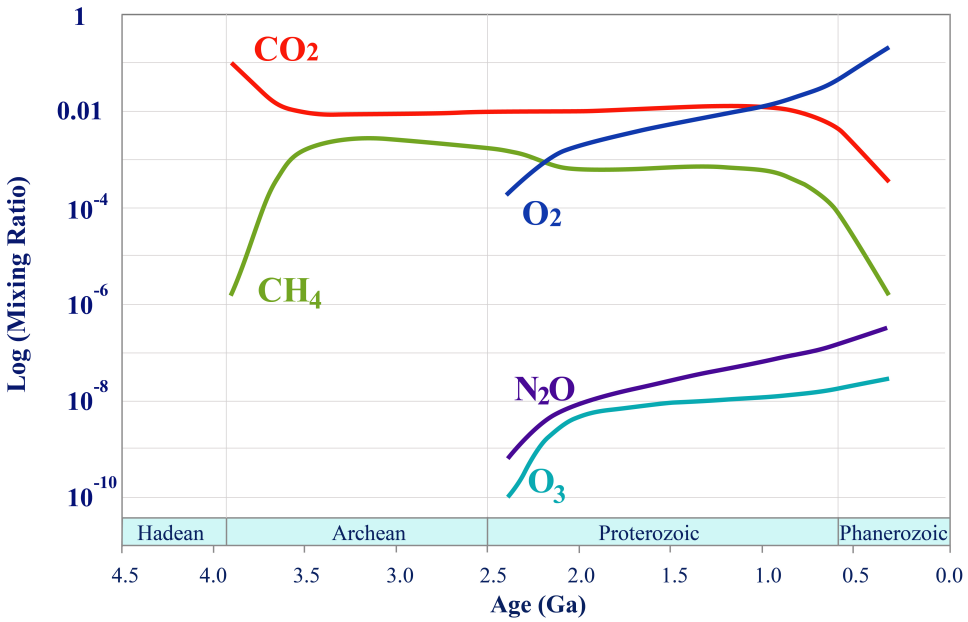

Figure 2-10: Schematic evolution of abundances of key atmospheric species over geologic time (after Kasting, 2004). The onset of the current, Phanerozoic eon is marked by the evolution of complex life forms at the start of the Cambrian period exemplified by trilobites and nautiloids.

While deepening our understanding of the variety and prevalence of various exoplanet atmospheric phenomena is fascinating in and of itself, the detection of biomarkers is a particularly rich scientific prize. Candidate biomarker gases are H_2O, CO_2, CH_4, O_3 and O_2, (e.g., Schindler & Kasting, 2000, Kaltenegger et al., 2007). Sagan, et al. (1993) found both O_2 and CH_4 to be in strong disequilibrium in observations of the Earth with the Galileo spacecraft, evidently the signature of a disequilibrium maintained by bioactivity (see Figure 2-10).

Several ambitious projects have been proposed – TPF-I (Beichman, 2006), Darwin (Cockell, 2009), very large area (10,000 m^2) flux collectors (Snellen, 2013)[1] – to detect the atmospheric signature of biomarker constituents of exoplanet atmospheres. However, the possibility of using the GMT, which is already well into development, to find the first evidence of exobiotic activity should be explored quantitatively. Techniques exploiting high dispersion spectroscopy to discriminate telluric and exoplanetary atmospheric signals have been demonstrated to have enormous potential (Snellen et al., 2010, Brogi et al., 2012, Rodler et al., 2012). Snellen has pointed out that the transmission signal of

[1] Both the TPFs and Darwin have been cancelled.

O_2 from an Earth-twin orbiting a M5 dwarf is only a factor of three smaller than that of carbon monoxide recently detected in the hot Jupiter τ Boötis b.

However, telluric absorption blankets most of the bands that these biomarker species might be observed in from ground based observatories and these features are only observable from space based observatories with considerably smaller apertures than the GMT. A particularly favorable opportunity exists in the O_2 A-band at 7600Å, where narrow telluric foreground features may be resolved and discriminated from exoplanet absorption features which are Doppler shifted with respect to the telluric features. This opportunity to detect O_2 as a biomarker is discussed extensively in Rodler and Lopez Morales (2013) and Snellen et al. (2013). The A-band is a better channel to exploit than the O_2 band at 1.2680μ given the comparable noise properties of CCDs and infrared arrays, except for the latest M type stars (i.e., M9). There are 55 strong lines in the A-band.

2.2.1.2. Detecting O_2

The O_2 A-band is a particularly powerful diagnostic of exobiotic activity for several reasons:

- The features are narrow and the relative motions of the Earth and an exoplanet Doppler shift the exoplanetary features out of the telluric absorption bands.
- The absorption features lie between 7600Å and 7700Å, where CCDs work particularly well and fringing is not an issue.

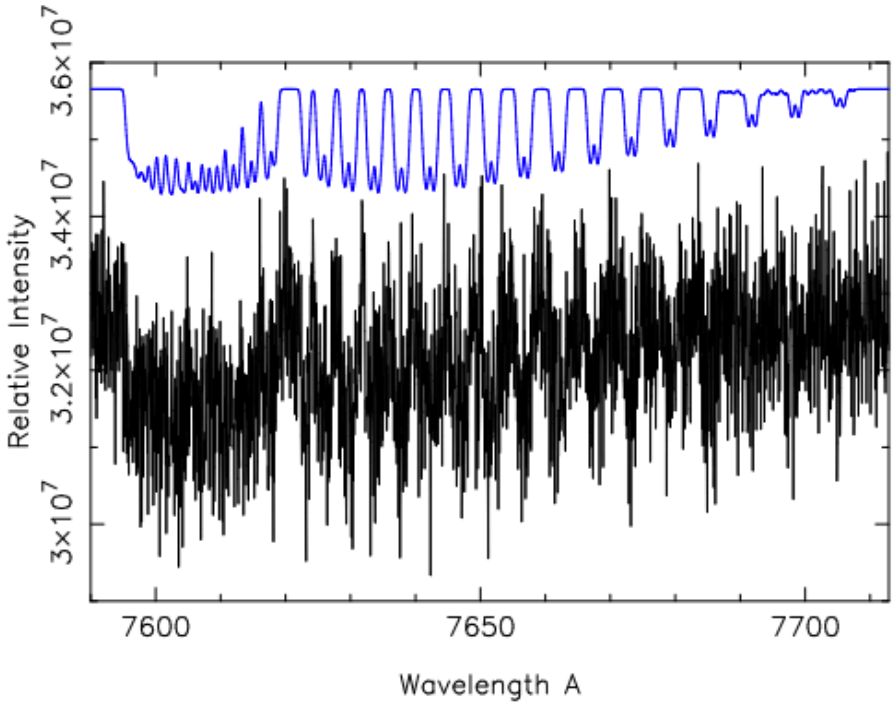

Figure 2-11: O_2 A-band theoretical spectrum of an Earth-like planet transiting a $0.1R_\odot$ star. The corresponding noise-free spectrum is shown, offset for illustration. The spectral S/N ratio is 18,000 per pixel, the spectral resolution (FWHM) is 7.7 km/s and the pixel size is 0.06Å (from Webb & Wormleaton, 2001).

Several groups have investigated the efficacy of various E-ELTs for the detection of exoplanetary O_2. An example of a modeling effort in support of the MUTHR spectrograph, which was proposed for the TMT appears in Figure 2-11. Snellen et al. (2013) extended previous predictions (Schneider (1994), Webb & Wormleaton (2001), Kaltenegger & Traub (2009) of O_2 detectability to that possible with a R=100,000 optical spectrograph on a 39m diameter E-ELT[2].

Snellen's group has pioneered the use of cross-correlation for the detection of exoplanetary molecular species by cross-correlating features within a molecular band. Figure 2-12 shows an example based on the GJ1214 system observed with R=100,000 spectrograph on a 39m E-ELT with a total throughput of 20%. GJ1214 is a M4.5 red dwarf 15 pc from the Earth with an apparent R magnitude of 13.8, which hosts a $6.55M_{Earth}$ super-Earth. Their conclusion is that a 3.8σ detection of O_2 could be achieved in 30 transits for an Earth-twin.

[2] No such instrument is currently planned for either the E-ELT or TMT.

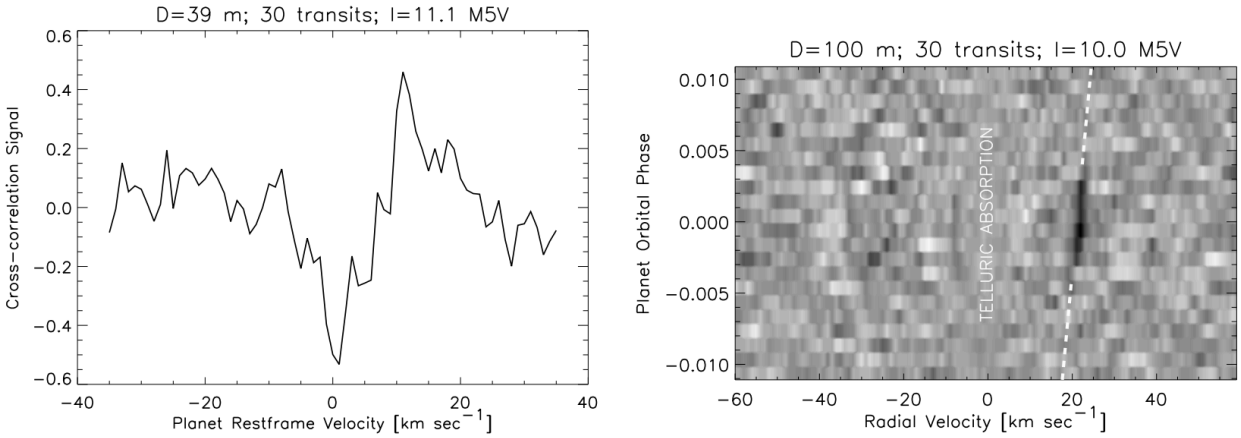

Figure 2-12: The left panel shows a simulated O_2 signal from a hypothetical Earth-twin in the GJ1214 system with the E-ELT and an R=100,000 spectrograph. The right panel shows the O_2 cross-correlation signal as a function of orbital phase for 30 transit observations of a similar system with a 100m flux collector (from Snellen, et al, 2013).

2.2.1.3. Detecting Exoplanetary O_2 with G-CLEF

More recently, Rodler & Lopez-Morales (2013, henceforth R&L), have improved on Snellen et al.'s modeling and considered the case of the GMT instrumented with G-CLEF. This exercise models many observational effects including random and correlated observational noise arising in the atmosphere and instrument, as well as refraction effects in the exoplanet atmosphere. The various spectral inputs of a sample system from their modeling is shown in Figure 2-13.

One important effect R&L have included in their modeling is that of exoplanet atmospheric refraction. Strong refraction in lower layers of the exoplanetary atmosphere will steer the beam of starlight out of the line of sight of a distant, terrestrial observer. This will alter the depth of absorption features. In the case of an Earth-Sun twin, the layers deeper than an altitude of 12-14 km will be invisible. In the case of lower mass stars, where the habitable zone is much closer to the host star, O_2 will be visible to an altitude 10 km above the planet surface.

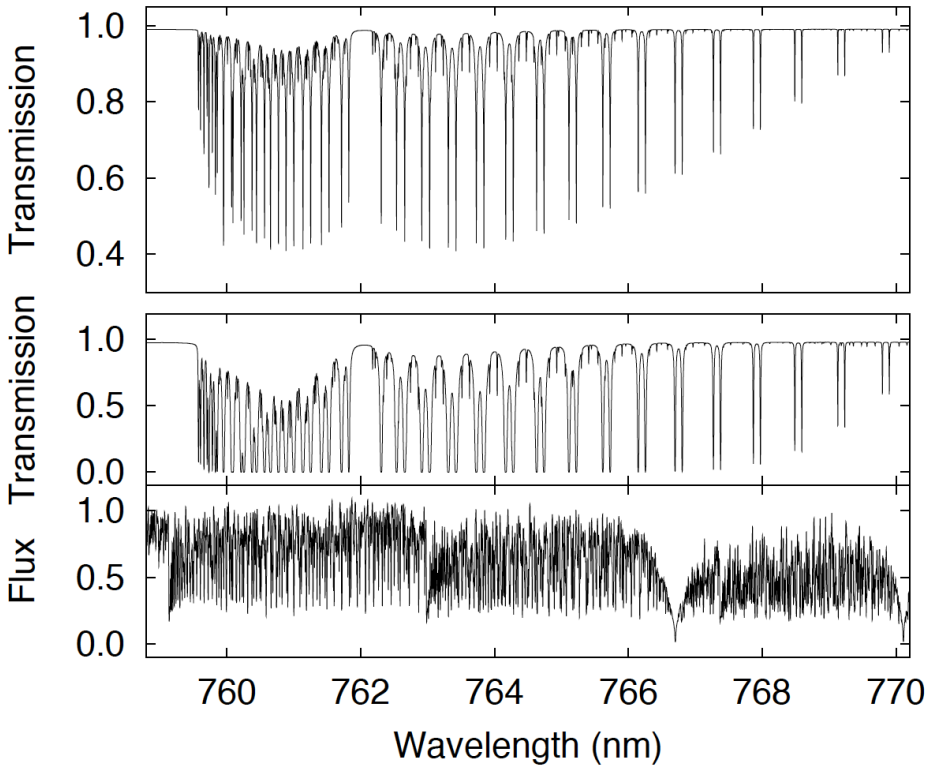

Figure 2-13: Top panel: transmission spectrum of the atmosphere of an Earth-like planet around 760 nm. Middle panel: telluric spectrum of our atmosphere for a zenith distance of 30° (airmass Z = 1.3). Bottom: PHOENIX model spectrum of an M4V star with a surface temperature of T = 3000° K, log g = 4.5 dex and solar abundance. All spectra are shown at a spectral resolution of R = 100, 000 (from Rodler & Lopez-Morales, 2013).

R&L and other authors have concluded that only M stars may be practically considered as viable targets for ground-based searched for the A-band signature of O_2 in the habitable zone. This is demonstrated in Table 2-4, which presents the properties of M1V to M9V stars and compares them a G2V. The tabulated parameter ϵ is the ratio of the area of the stellar disk to the detectable atmospheric ring in a Earth-twin when proper account of the exoplanet's atmosphere refractive properties has been taken. It can be seen that this ratio is extremely large for solar type stars, which will significantly dilute the exoplanet O_2 signal. It is also to be noted that as the stellar mass decreases, the period also decreases owing to the reduced diameter of the habitable zone. The increased frequency of transit events vastly improves the observability of transits. While the brightness of target stars decreases with mass, the decrease in ϵ more than compensates this effect.

Type	T_{Eff} (K)	R($R_\odot$)	ϵ	M_I(Mag)	P (d)	Transit Duration (h)
G2V	5800	1.00	520000	4.1	365	13.1
M1V	3600	0.49	125000	7.7	43	4.0
M2V	3400	0.44	101000	8.3	33	3.4
M3V	3250	0.39	80000	8.8	27	3.0
M4V	3100	0.26	35000	10.0	16	2.1
M5V	2800	0.20	21000	11.2	9.5	1.5
M6V	2600	0.15	12000	12.4	6	1.1
M7V	2500	0.12	7500	13.6	4.1	0.78
M8V	2400	0.10	6000	13.9	3.3	0.69
M9V	2300	0.08	4000	14.7	1.9	0.43

Table 2-4: Host star and habitable zone planet parameters. ϵ is $A_{Star}/A_{Atm.Ring}$. M_I is at a distance of 10 pc (from Rodler & Lopez-Morales, 2013).

A further consideration is the effect of blending of telluric and exoplanet features as a function of Doppler shift or relative radial velocity. This effect is shown in Figure 2-14, where the fraction of blended lines is plotted as a function of the mutual line of sight velocity. An optimal range of relative velocities is 15 to 30 m/s. For velocities inside the +/- 15 m/s band, many telluric and intrinsic O_2 features will be blended. Another favorable band exists between 65 and 85 km/sec. It should be emphasized that these velocities depend on the velocity of the star with respect to the barycenter, and the line of sight with respect to terrestrial rotation and the Earth's orbit at the time of observation.

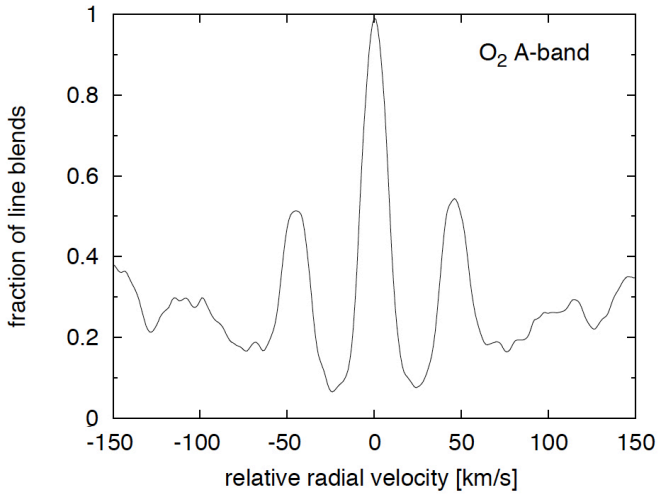

Figure 2-14: Plot showing the normalized fraction of line blends between the telluric spectrum and the transmission spectrum of the Earth twin as a function of the relative radial velocity between the host star and Earth (from Rodler & Lopez-Morales, 2013).

R&L have also parameterized the effect of correlated (red) noise on observation time. Red noise is related to instrumental and atmospheric effects – e.g. variations of the airmass or changes of position on the spectrograph detector. This parameterization is plotted in Figure 2-15, i.e. the observation time multiplier as a function of red noise contribution. As an example a red noise contribution of 0.4 increases the required observation time by a factor of 2. Typical red noise contribution for ground based optical observations is 0.2 and between 0.5 and 1.0 in the near-infrared. This confers a considerable advantage to the optical band.

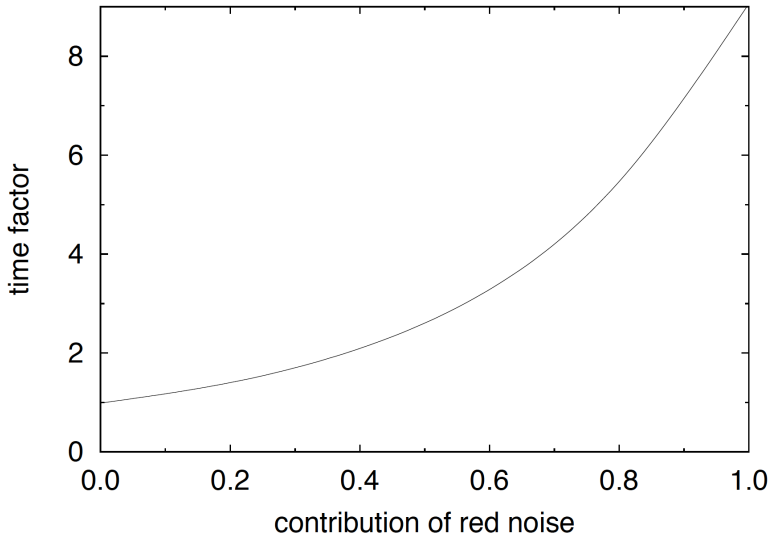

Figure 2-15: The effect of red noise on the number of transits and the amount of time necessary to detect O_2 in the atmosphere of an Earth twin at a 3σ confidence level. (from Rodler & Lopez-Morales, 2013).

The performance of G-CLEF for the detection of exoplanetary O_2 as a function of spectral type is summarized in Table 2-5 and Figure 2-16. The exposure times have been calculated using the G-CLEF Prototype Exposure Time Calculator (PETC). The resolution of G-CLEF is taken to be 100,000. This could be provided in the image-sliced, high-resolution (HR) mode. However, the HR mode is currently envisioned to be R~150,000, so further modeling is required to determine the effect on O_2 detection. Median seeing is assumed (0.8 arcsec) and air masses are distributed between Z=1.1 to 2.0. The required significance is 3σ.

Type	Obs. Time (h)	Duty Cycle	Transits	Time (years)
G2V	470	0.18	37	37
M1V	133	0.86	33	35
M2V	133	0.91	40	31
M3V	130	0.94	44	28

M4V	70	0.98	34	14
M5V	79	0.98	53	12
M6V	75	0.98	68	10
M7V	61	0.98	78	8
M8V	69	0.98	100	8
M9V	67	0.98	154	7

Table 2-5: Simulations of G-CLEF performance on the GMT (from Rodler & Lopez-Morales, 2013).

Since the target stars will be very bright, the integrations will be very short to avoid driving the CCD into a non-linear regime (assumed to be 36,000 ADU for G-CLEF). For this reason, the read-time has an impact on observing efficiency or "duty cycle" in Table 2-5. For the purposes of their study, R&L assumed a dead time between exposures of 15 seconds and a read out noise (RON) of 5 e^-. While these seem like realizable operating parameters for a modern CCD and CCD controller, other programs will probably prefer to reduce read-out rate to achieve lower RON. The read out rate will then need to be easily adjustable.

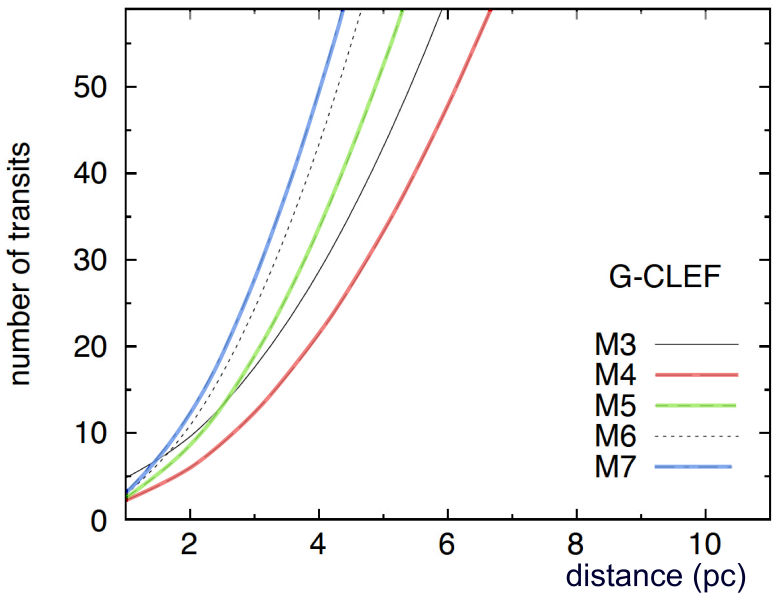

Figure 2-16: Number of transits required to measure the 760 nm oxygen absorption band with G-CLEF on the GMT with 3σ confidence versus distance of the planetary system from Earth (from Rodler & Lopez-Morales, 2013).

The range of observable stellar types in Table 2-5 extends from approximately M4 to M9. R&L have

studied the tradeoff between G-CLEF observing in the 7600Å band and a hypothetical near-infrared instrument observing the 1.27μ band. For the purposes of comparison both instruments are operated on a 39m E-ELT. The results of this comparison are plotted in Figure 2-17, where the observing time required for detection of O_2 in the atmosphere of an exoplanet orbiting a M8 & M9 star is parameterized as a function of distance to the star. While the near-infrared instrument outperforms G-CLEF in the case of a M9 star, G-CLEF detects O_2 in a considerably shorter time for the M8 case when the effects of red noise are included.

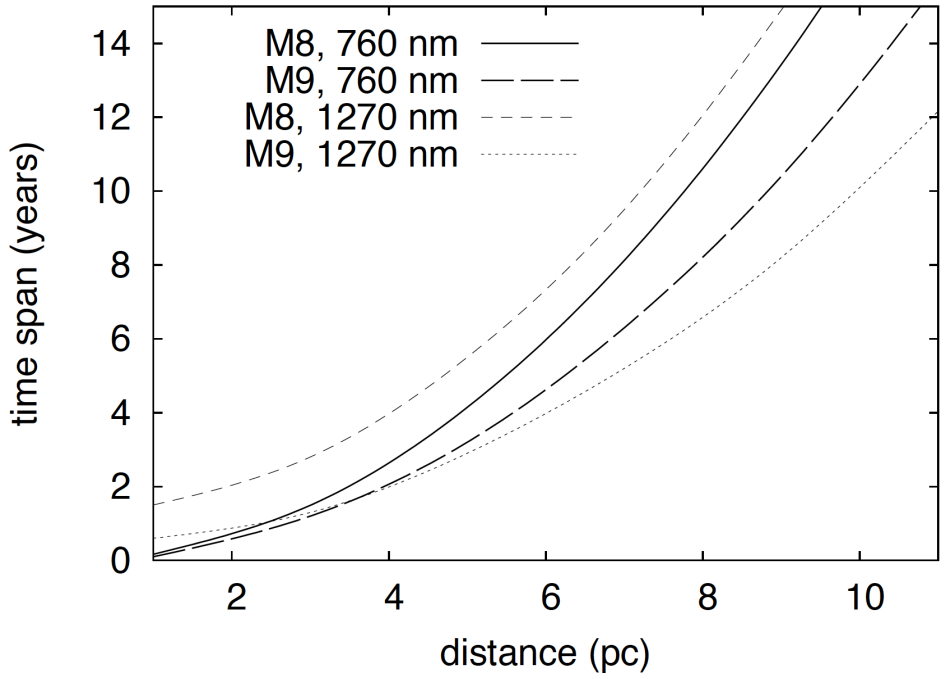

Figure 2-17: Time span of the observations versus distance of the host star for observations of M8V and M9V stars in the O_2 A-band at 7600 Å and the O_2 band at 1.27 μ. The observations at 7600 Å have a red noise level of 20%, while the observations at 1.27 μ have a red noise level of 50% of the white noise level. Unlike the ideal case of no red noise, the observations in the O_2 band at 1.27 μ are more efficient than the observations on the O_2 A-band only for M9V stars. These results are based on SIMPLE and a G-CLEF-like instrument mounted on the E-ELT. (from Rodler & Lopez-Morales, 2013).

R&L have limited their study to consider stars to a maximum distance of 20 pc. The frequency of stars as a function of subtype is plotted in Figure 2-18, for a volume within 5 pc and 10 pc. The census of nearby M stars is dominated by M3, M4 & M5 subtypes, and these are quite numerous.

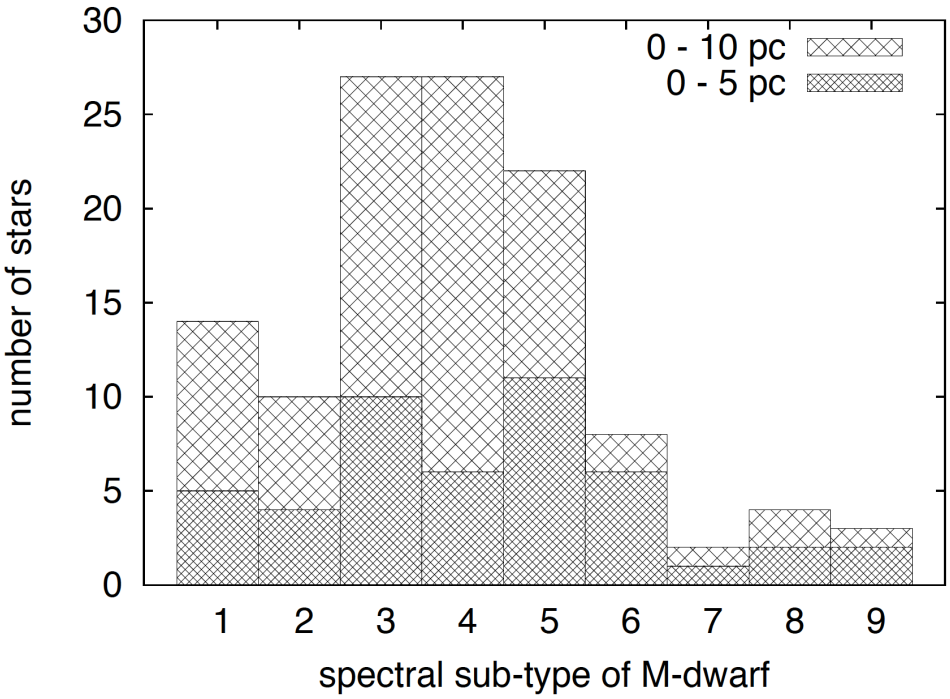

Figure 2-18: Frequency of M-dwarfs in the solar neighbourhood (distances d ≤10 pc) as a function of spectral type. The most common sub-types are M3 and M4 dwarfs. For distances up to 5 pc, the most frequent sub-types are M3 and M5 dwarfs. (from Rodler & Lopez-Morales, 2013).

Another issue affecting the sample of potential targets stars is that of radial velocity, where L&R showed that for the line of sight velocity interval between +15 km/sec and -15 km/sec, blending of telluric and exoplanetary O_2 features compromises detectability (Figure 2-14). A histogram of the percentage of M stars in radial velocity intervals is shown in Figure 2-19. While 56.8% of M stars in the solar neighborhood have radial velocities in ±15 km/sec band and 44.3% are within a ±10 km/sec band, a proper treatment of Earth motion must be made to assess the impact of these statistics on the search for O_2 in exoplanet atmospheres. The semi-amplitude Earth velocity with respect to the barycenter is 29.8 km/s. The radial velocity shift of a star resulting from the Earth's motion depends on ecliptic latitude (β) where:

$$V_{Bary} = 29.8 \cdot Cos(\beta) \frac{km}{s}$$

For the vast majority of stars, V_{Bary} is between 20 & 29.8 km/s. An example of the observability of a sample object with V_{Bary} 10, 20 & 30 km/sec is plotted in Figure 2-20. The fraction of observable time is calculated assuming the object is above 2 airmasses, the sun is 15° below the horizon, and the net radial velocity is between 15 and 30 km/s. This conclusion drawn from this is that atmospheric

lines would be detectable 20% - 40% of the time for the majority of M dwarfs, even though their intrinsic radial velocities are between -15 and 15 km/s.

Rodler and Lopez-Morales conclude that "... successful measurements of O_2 in Earth-like atmospheres with future ground-based instrumentation will be most likely limited to host stars of spectral types later than M3V, which are located at distances less than 8 pc."

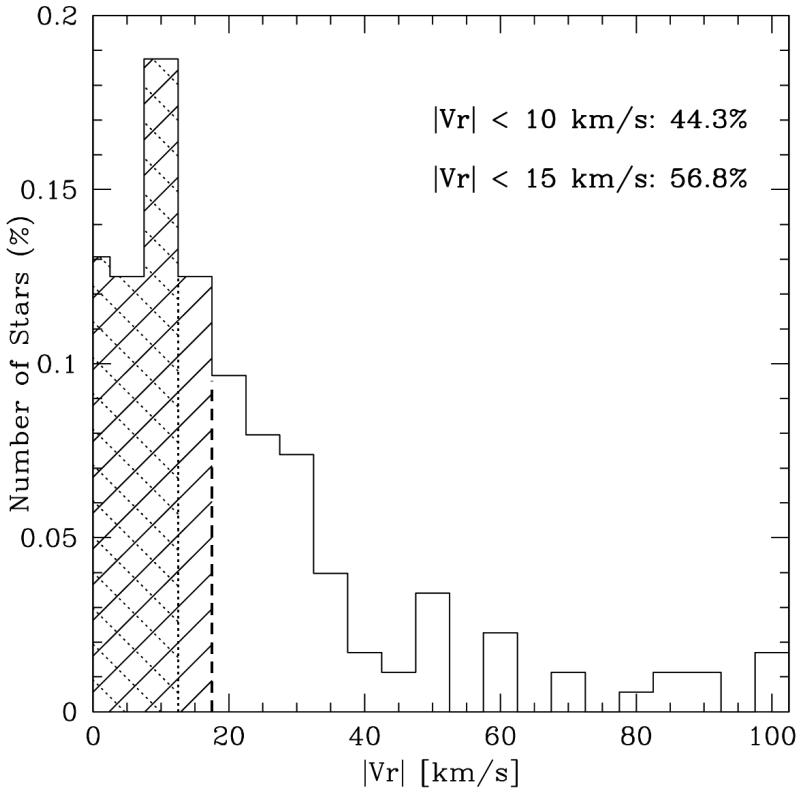

Figure 2-19: Histogram of the distribution of barycentric radial velocities for a sample of 176 M-dwarfs published by Chubak et al. (2012) in 5 km/s bins. The bins of stars with velocities less than 15 and 10 km/s, respectively, are shown as dashed and square shaded areas in the histogram. Assuming the Chubak et al. (2012) sample is representative of all nearby M-dwarfs, about 44.3% of the stars will have absolute radial velocities smaller than 10 km/s, and 56.8% will have radial velocities smaller than 15 km/s (from Rodler & Lopez-Morales, 2013).

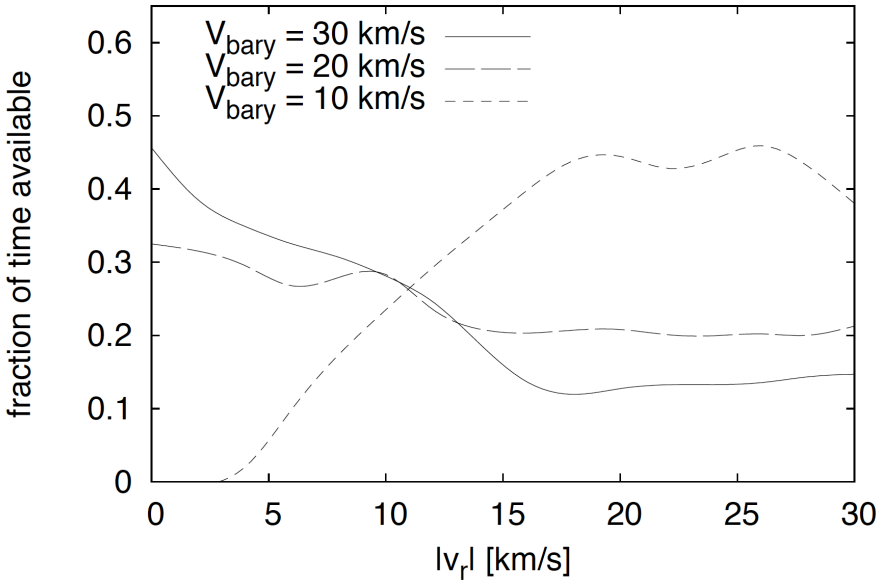

Figure 2-20: Amount of time of optimum visibility of an object in units of the yearly observing time available at an ideal observing site as a function of the absolute value of the systemic radial velocity $|v_r|$. We only consider the target to be visible when the following criteria are fulfilled: (a) air mass $X \leq 2$, (b) Sun is 15° below horizon, and (c) a relative radial velocity of ±(15 to 30) km/s. We note that the vast majority of stars exhibit semi-amplitudes of the barycentric velocity of $V_{Bary} > 20$ km/s (from Rodler & Lopez-Morales, 2013).

2.2.2. Science Requirements (Level 1 Requirements)

- Observe exoplanet atmospheres in transmission, emission and reflection
- Measure phase relationship between orbital motion and thermal emission
- Measure red continuum of exoplanets to observed cloud dust scattering
- Observe exoplanet molecular spectral features

The targets are expected to be dwarfs of class M3 to M8 within 20 pc of the Sun. This implies a magnitude range of M_I =6.13 to 18. The bright end of this distribution is set by one of the brightest M dwarf visible from Las Campanas GJ 229. The faint end is set by the brightness of an M8 star at a distance of 20 pc.

Transits are brief but occur at specific times, so it is essential that G-CLEF and the GMT have the capability to observe time series Targets of Opportunity (TOOs) flexibly. The duration of transits is hours to half-hours. Presumably the observation must include observations adequately sampling spectra before and after transit, so an observation of a transit of 1 – 4 hours duration is required.

The target stars may in some case be extremely bright, so it is essential that GMT + G-CLEF have the capability of guiding on and acquiring data from bright stars.

The data G-CLEF yields should make it possible to detect the presence of O_2 A-band features by the spectral and temporal cross correlation. The data should be of a quality such that the various features with the A-band may be cross correlated and the sequential spectra stack so that the information in the time sequence may be exploited to extract the O_2 signal from the noise and the telluric features. The spectral features are quite narrow and must be resolvable from foreground telluric feature. These features all lie in a fairly narrow passband between 7600Å & 7700 Å.

It is also to be noted that it is desirable to execute the science program in as short a time as possible. We include a M3 star at a distance of 10 pc, however the pessimistic prediction of R & L is that this will require a 28 year long science program. Any reduction in this time and extension to M1 or M2 types is extremely desirable.

#	Requirement
2.2.1	G-CLEF shall have good sensitivity in the O_2 A-band (7600-7700Å) passband.
2.2.2	G-CLEF shall have the capability to distinguish intrinsic and telluric molecular species with velocity differential of 1 m/s or greater.
2.2.3	G-CLEF shall have good continuum sensitivity in the 6000Å-1μ passband.
2.2.4	G-CLEF, as deployed on the GMT, shall be capable of observing extremely bright stars efficiently, potentially $M_I = 6.13$
2.2.5	G-CLEF shall be capable of measuring the radial velocity of a large sample of stars with the cadence necessary to distinguish intrinsic and telluric absorption molecular absorption features.

Table 2-6: G-CLEF Science Requirements (Level 1 Requirements) to enable exoplanet atmosphere observations.

2.2.3. References

Bean, J.L., et al., 2013, Ground Based Transit Spectroscopy of the Hot-Jupiter WASP-19B in the Near-Infrared, ApJ, 771, 108

Bean, J., Kempton, E. & Homeier, D., 2010, A Ground-Based Transmission Spectrum of the Super-Earth Exoplanet GJ 1214b, Nature, 468, 669

Beichman et al., 2006, Status of the terrestrial planet finder interferometer (TPF-I), SPIE, 62680S, 25

Brogi, M. et al. 2012, The signature of orbital motion from the dayside of the planet τ Boötis b, Nature, 486, 502

Chubak, et al., 2012, Precise Radial Velocities of 2046 Nearby FGKM Stars and 131 Standards, ApJS, Submitted

Cockell et al., 2009, Darwin-A Mission to Detect and Search for Life on Extrasolar Planets, AsBio, 9, 1.

de Mooij, E.J.W. & Snellen, I.A.G. 2009, Ground-based K-band detection of thermal emission from the exoplanet TrES-3b, A&A, 493L, 35

Fressin, F., et al. 2013, The False Positive Rate of Kepler and the Occurrence of Planets, ApJ, 766, 81.

Jordan, A. et al., 2013, A Ground-Based Optical Transmission Spectrum of WASP-6b, ApJ, Submitted.

Kaltenegger, L. & Traub, W.A., 2009, Transits of Earth-like Planets, ApJ, 698, 519

Kaltenegger, L., Traub, W.A. & Jucks, K.W., 2007, Spectral Evolution of an Earth-like Planet, ApJ, 658, 598

Rodler, F. & Lopez-Morales, M. 2013, Feasibility Studies for the Detection of O_2 in an Earthlike Exoplanet ApJ, Submitted.

Rodler, F., Lopez-Morales, M. & Ribas, I. 2012, Weighing the Non-transiting Hot Jupiter τ Boo b, ApJ, 753L, 25.

Sagan, C., et al. 1993, A Search for Life on Earth with the Galileo Spacecraft, Nature, 365, 715

Schindler, T.L. & Kasting, J.F., 2000, Synthetic Spectra of Simulated Terrestrial Atmospheres Containing Possible Biomarker Gases, Icarus, 145, 262

Schneider, J., 1994, On the search for O2 in extrasolar planets, Ap&SS, 212, 321

Sing, D.K. & Lopez-Morales, M. 2009, Determining Atmospheric Conditions at the Terminator of the Hot Jupiter HD 209458b, A&A, 493L, 31

Snellen, I, et al., 2013, Finding Extraterrestrial Life Using Ground-based High-dispersion Spectroscopy, ApJ, 764, 182.

Snellen, I., et al., 2010, The orbital motion, absolute mass and high-altitude winds of exoplanet HD209458b, Nature, 465, 1049

Webb, J.K. & Wormleaton, I., 2001, Could We Detect O_2 in the Atmosphere of a Transiting Extra-solar Earth-like Planet?, PASA, 18, 252

3. Stellar astrophysics: exploring the Milky Way and Local Group

3.1. Documenting the nucleosynthetic yields of the first stars

3.1.1. Science Drivers (Level 0 Requirements)

3.1.1.1. Introduction

Studying old, metal-poor stars allows for connecting the present state of the Galactic halo (characterized by halo kinematics and/or very low metallicity) with its long-lasting assembly history. By retaining the chemical information from their formation time in their atmospheres, these low-mass (M ~ $0.8M_{\odot}$) stars also enable the reconstruction of the chemical evolution, early star formation, and galaxy evolution ("stellar archaeology"; Beers & Christlieb 2005, Frebel & Norris 2013). Detailed abundance information of the most metal-poor stars, paired with nucleosynthesis calculations, enables the only available diagnostic to study the nature of the first stars and their massive supernovae, the early chemical evolution of the Galaxy, and the history of star formation in the Milky Way. Taken altogether, these stars are an exceptionally versatile tool for investigating the conditions of the early universe and the assembly processes of large galaxies because they are the easily accessible local equivalent of the high-redshift universe. Hence, these stars provide an opportunity to learn about those high-redshift epochs of early star and galaxy formation which are beyond the reach of any direct observations (e.g., JWST; Panagio 2003).

Progress can be made through the study of ultra metal-poor stars with [Fe/H]<-4. Their abundances can be interpreted as a result of just one nucleosynthesis event (i.e. one Pop III supernova; Christlieb et al. 2002, Frebel et al. 2005) that occurred prior to the star's formation. Together with simulations of nucleosynthesis, supernovae, metal-mixing processes, star formation and early galaxy formation a comprehensive array of topics regarding the nature of the early universe can be addressed (e.g. Cayrel et al 2004, Barklem et al. 2005, Cohen et al 2007, McWilliam et al 1995). Only sufficient amounts of data such as the those from [Fe/H]<-4.0 stars can provide unique insight into:

- The primordial stellar mass function (IMF)
- The first supernovae (SNe), their yields and explosion properties (energy, ejected mass, mixing)
- The critical metallicity for transition from Pop III to Pop II
- The role of reionisation on galactic evolution
- The origin and evolution of the elements and the associated nucleosynthesis processes
- The efficiency of gas mixing in the early Galaxy

Moreover, the interpretation of the abundance data provides important constraints on cosmological simulations of early star and galaxy formation, the hierarchical assembly of galaxy formation and the build up of the Galactic halo and large galaxies more generally (e.g. Frebel & Bromm 2012).

3.1.1.2. Discovering the most metal-poor stars

Searches for the chemically most primitive stars have been ongoing for decades (Bond 1981, Beers et al. 1992, 1999, Wisotzki et al. 2000, Christlieb 2003) and by now half a dozen stars are known with [Fe/H] <-4.0. Two stars even have [Fe/H] <-5.0 and there is a new discovery of a star with [Fe/H] <-7.0. Their abundance signatures provide unprecedented constraints on theoretical models of the first stars and SNe, and early star- and galaxy formation. Their discoveries were, in part, due to new surveys and analysis methods that are pushing forward to find more of these exquisitely rare objects with substantially higher efficiency than previous searches (e.g. SkyMapper; Keller et al. 2007).

Large surveys (e.g., HK survey, Hamburg/ESO survey, SDSS, SkyMapper, APOGEE, GALAH) are required to provide low or medium resolution spectra or narrow-band photometry to search for weak-lined, metal-poor stellar candidates. Those data have to cover the strong Ca II K line at 3933Å because the strength of this line indicates the metallicity of the star. If this line is sufficiently weak as a function of the star's estimated effective temperature, an object is selected as a candidate metal-poor star. For all candidates medium-resolution spectra are required to more accurately determine the Ca II K line strength for a more robust estimate of the Fe abundance.

To confirm the metallicity and to measure the elemental abundances including that of iron, high-resolution optical spectroscopy is required (see Table 3-1). Only then the weak elemental absorption lines become detectable enabling abundance measurements. Those elements include carbon, magnesium, calcium, titanium, nickel, strontium, and barium. They trace different enrichment mechanisms, events and timescales. Abundance ratios [X/Fe] as a function of [Fe/H] can then be derived for the lighter elements (Z < 30) and neutron-capture elements (Z > 38). The final number of elements hereby depends on the type of metal-poor star, the wavelength coverage of the data, and the data quality itself.

The last step in identifying truly metal poor stars - high-resolution spectroscopic observations of potentially metal-depleted stars that have passed the sieve of lower resolution study - have been successfully obtained with the largest available telescopes (Magellan, the VLT, Subaru, and Keck, as well as from space with HST). The resulting abundance data has been sufficient for comparisons with theoretical nucleosynthesis calculations and laboratory measurements. However, this is only true for a small fraction of the potential sample. There are many more candidates than follow-up opportunities, and even more importantly, many of the most interesting candidates are too faint to obtain high signal-to-noise (S/N), high resolution spectra with instruments available at existing telescopes. Larger apertures are required to make significant progress in this field.

Given the new surveys and their initial successes, it is obvious that this decade will see an explosion of candidate ultra-metal-poor stars. Hence, this will deliver on the promise of ultra-metal-poor stars constraining the physics of the early Universe and the properties of the first stars. Especially the SkyMapper Southern Sky Survey (Keller et al. 2007) is expected to provide a 100-fold increase in the numbers of [Fe/H]<-3 stars compared to existing numbers, and also dozens of objects with [Fe/H]<-4.0. Similar results may be expected from the LAMOST (Li et al., 2010) and

HERMES/GALAH multi-object spectroscopic surveys. The advent of LSST will also enable the search for increasingly fainter metal-poor star candidates.

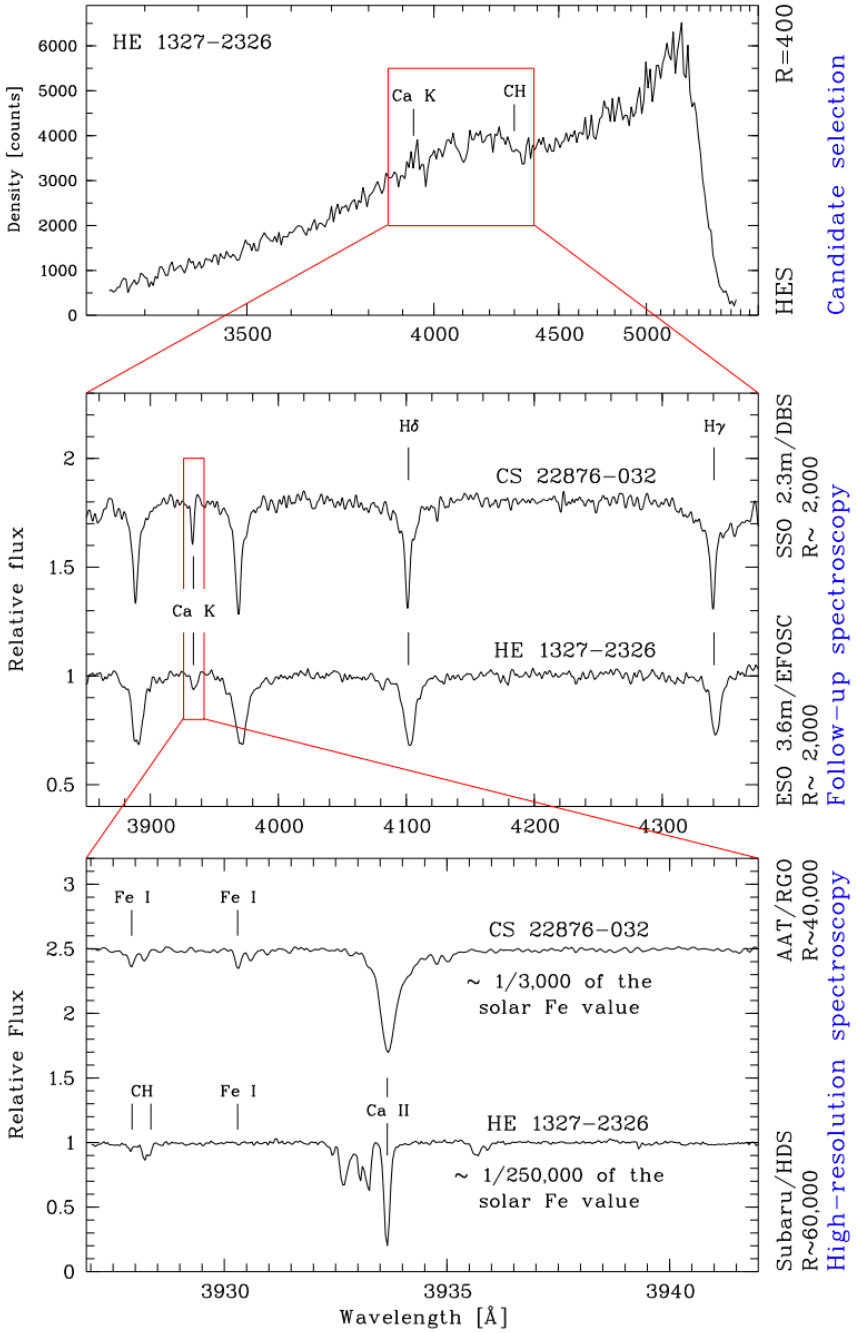

Figure 3-1: The three traditional steps of isolating the most metal-poor stars, starting with low resolution survey data for initial candidate selection, confirming Fe values with a Ca II K calibration

at medium resolution and obtaining a full set of chemical abundances from a high-resolution spectrum. From Frebel 2005.

3.1.1.3. Detecting the weakest absorption lines in low-metallicity stellar spectra with G-CLEF

Given the upcoming "decade of surveys" that will reach to very faint magnitudes, i.e. the majority of new metal-poor candidates will be too faint for high-resolution follow-up with existing 6-10m telescopes. The realistic limit to carry out a high-resolution survey to characterize the metal-poor tail of the metallicity distribution function is currently g~16. Even those data are in most cases not of sufficient S/N for the required in-depth analyses. The very hard limit for high-resolution, high-S/N spectroscopy for detailed chemical abundances is thus 16-17th magnitude. This is where the outer halo only begins. Many candidates from the Hamburg/ESO survey, Skymapper, LAMOST and most of SDSS targets are in this brightness regime and fainter. The problem is worsened by the fact that the most metal-poor stars have extremely weak lines. Hence, low S/N is not adequate, as many absorption lines will at best be a equivalent widths of a few mA. The new discovery of a star with [Fe/H]<-7.0 (Keller et al. 2014) illustrates this point: *No Fe lines* are detected in the spectrum of this g~15 star despite a ~10h exposure yielding a spectrum with S/N~100. If there is any iron present in this star, the strongest Fe lines have equivalent widths much less than 1mÅ.

As a consequence, the outer halo remains a spectroscopically largely unexplored territory. However, metal-poor star and kinematic studies, as well as a large range of theoretical works, suggest that the most metal-poor stars may be more easily found further out, as the density of metal-rich stars decreases rapidly and the number of metal-poor stars increases. On the other hand, many g<16 stars are known to have unusual chemical abundance patterns (including stars with [Fe/H]<-7.0) that would require very high S/N spectra for their detailed analysis. Again, with current facilities, only very bright stars can be observed with a S/N of 500 or more, thus limiting our ability to use these stars to learn about the origin and evolution of the elements and limiting the comparison with SN nucleosynthesis model predictions.

In summary, only with a high-resolution spectrograph such as G-CLEF on the GMT can the current limitation on high-resolution spectra be overcome. By the time G-CLEF has first light, the current surveys will have produced a long list of excellent most metal-poor stellar candidates ready for detailed chemical abundance analyses. The results will provide major advances in our knowledge of the early universe.

3.1.2. Science Requirements (Level 1 Requirements)

G-CLEF will make major contributions to stellar archaeology through a two-component observing program. A discovery mode employing lower quality snapshot spectra (R~20,000, S/N~30 at 4000Å) will confirm the metallicity of the pre-selected targets and quickly identify any unusual abundance characteristics. The most important targets will then be observed with higher resolution (R~40,000) and high S/N (~100 per resolution element or until Fe lines are detected, depending on the nature and metallicity of the object) to acquire data required for a detailed chemical abundance

analysis.

An average candidate is expected to have g~18 which is currently an unexplored regime in terms of high-resolution spectroscopy. These observations can be made in a variety of seeing condition, lunar phases, sky clarity, and observing season. Good wavelength coverage in the blue is crucial since the strongest Fe lines and the Ca K line are located there. The S/N in this region will drive the overall exposure times. Indeed, even with the GMT, long exposures are required. Assuming 0.8" seeing 15h is required to obtain a S/N = 100 spectrum on a g=18 star with a 7 mirror GMT. Table 3-1 lists exposure times for the snapshot and high S/N spectra for both the 4 and 7 mirror cases and several magnitudes. Even though exposure times are long, sub-exposures over several nights can be summed to reach the required S/N.

Brighter candidates are also expected to be found, which offers more observational flexibility and required exposure times on the targets. Moreover, cutting edge science can be already done with observations of individual stars. While ultimately a large sample of [Fe/H]<-4.0 stars is required to fully maximize the potential of these objects to constrain early universe science, history shows that good data for even just one exceptional star (such as measuring the true iron abundance level of a [Fe/H]<-7.0) can have important ramifications for our understanding of the earliest supernovae (e.g. Heger & Woosley 2010). Hence, obtaining high-resolution spectra of a small sample of 5 stars with 18 mag would thus take a total of 0.5 nights to confirm their metal-poor nature with snapshot spectroscopy and an additional ~5 nights for 3 high S/N spectra.

Making good use of small samples becomes important for the intermediate stage of a 4 mirror GMT. Observations can then be limited to somewhat brighter magnitudes (~17mag) and/or fewer stars (see Table 3-1). High-resolution spectra of a sample of 5 stars with 17 mag (and 4 mirrors) would thus take a total of ~2 hours to confirm their metal-poor nature with snapshot spectroscopy and an additional ~2.5 nights for 3 high S/N spectra.

A larger long-term program of 250 snapshot spectra for stars with an average g=18 and with 7 mirrors would require about 20 nights with G-CLEF on GMT. High-resolution spectra of a selected subset of 20 stars will take an additional 30 nights.

g Mag	Res.	S/N	λ	T_{exp} (4 mirrors)	T_{exp} (7 mirrors)
18	40K	100	3850 Å	25 h	15 h
18	20K	30	4000 Å	80 min	45 min
17	40K	100	3850 Å	7 h	4 h
17	20K	30	4000 Å	25 min	15 min
16	40K	100	3850 Å	2.2 h	1.25 h

Table 3-1: Exposure times for snapshot and high resolution spectra for 4 and 7 mirrors assuming 0.8 arcsecond seeing.

Ultra metal-poor stars by definition have very weak absorption lines (few mA or less), so that very high quality (both in terms of spectral resolution and S/N ratio) spectra are required. Generally, spectroscopic line density increases with decreasing wavelength. In cool metal-rich stars the domain $\lambda < 4000$Å is too crowded for abundance analyses, but in ultra-metal-poor stars that same wavelength region often contains the only detectable transitions of some elements. For example, for the warm 6200K, [Fe/H]=-5.4, V=13.5 star HE1327-2326, 21h with UVES on VLT were required to barely detect and measure just a handful of Fe lines (all below 4000Å) as well as oxygen and nitrogen abundances (below 3400Å). In fact, 13 of the 24 detected lines with measurable EW in HE1327-2326 are below 3900Å. Figure 3-2 shows the strongest Fe line in HE1327-2326 – only a tiny line is left to detect, requiring a S/N of more than 100 per resolution element.

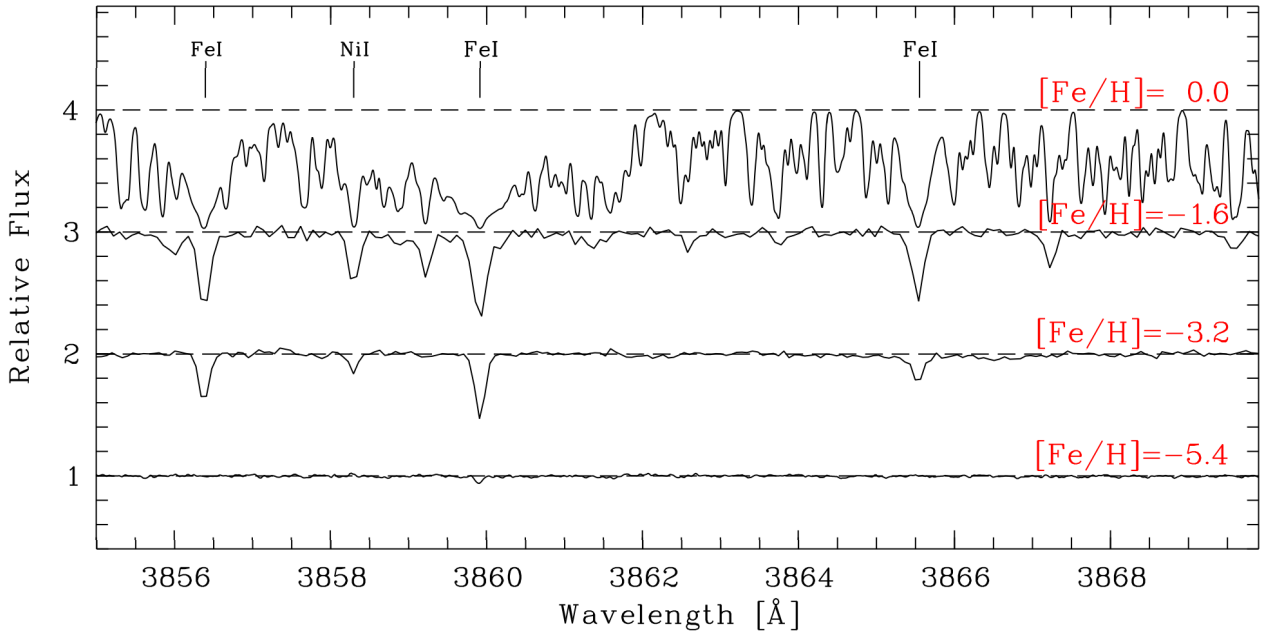

Table 3-2: Spectral comparison of metal-poor main-sequence stars. HE1327-2326 is shown at the bottom. The Fe line at 3859Å is the strongest line observed in the star. It has an equivalent width of ~6mÅ.

A key science program for G-CLEF is the detection and characterization of the most metal-poor stars in the outskirts of the Milky Way halo. These observations thus require good blue sensitivity to ~3500Å or less. Especially important lines are Fe I at 3859Å, Ni I at 3524Å, Ti II at 3759Å and 3761Å and various neutron-capture elements including uranium shortward of 4000Å. Since all these lines are extremely weak (equivalent width ~ few mA), the required resolution for these observations is 40,000 and high S/N is required (e.g., S/N ~ 100 per resolution element or more).

Given the long exposure times it is not possible to obtain the high S/N spectra for a given object in one night only. Queue scheduling will be required to observe a given star repeatedly to build up the

required S/N.

The Level 1 requirements for the study of extremely metal poor stars are summarized in **Error! Reference source not found.**

#	Requirement
3.1.1	G-CLEF shall have good sensitivity to at least 3500Å
3.1.1	G-CLEF shall be capable of resolving emission features with EW ~ 0.1 mÅ in 8 hours in the 3500 - 5300Å passband.
3.1.1	G-CLEF shall be capable of observing faint objects to 18th magnitude with good efficiency

Table 3-3: G-CLEF Science Requirements (Level 1 Requirements) for the detection and characterization of extremely metal poor stars

.

3.1.3. References

Barklem et al. 2005 A&A, 439, 129
Beers & Christlieb 2005, ARA&A, 43, 531
Beers et al. 1992, AJ, 103, 1987
Beers et al. 1999, AJ 177, 981
Bond 1981, ApJ 248, 606
Cayrel et al 2004, A&A, 416, 1117
Christlieb et al 2002, Nature, 419, 904
Christlieb 2003, Rev. Mod. Ast. 16, 191
Cohen et al 2007, ApJ, 659, 161
Frebel et al 2005, Nature, 434, 871
Frebel & Bromm 2013, ApJ, 759, 115
Frebel & Norris 2013, "Planets, Stars & Stellar Systems", by Springer
Heger & Woosley 2010, ApJ, 724, 341
Keller et al. 2007, PASA, 24, 1
Keller et al. 2014, Nature, in press
McWilliam et al 1995, AJ, 109, 2757
Norris et al 2007, ApJ, 670, 774
Panagia 2003, Chin. J. Astro. & Astroph. 3, 115

Wisotzki et al. 2000, A&A, 358, 77

3.2. The origin and history of the Milky Way's satellite galaxies: insight into early star and galaxy formation

3.2.1. Science Drivers (Level 0 Requirements)

3.2.1.1. Introduction

The chemical abundance patterns in stars that are not fully convective encode the entire previous history of the baryonic material that formed the star. Observations of these chemical abundances therefore have the potential to place constraints on an enormous range of issues, from primordial nucleosynthesis (Spite & Spite 1982) to supernova yields (Cayrel et al. 2004) and the star formation history of the galaxy in which the star lives (Venn et al. 2004). The oldest, most metal-poor stars are particularly interesting probes because they represent the local equivalent of the high-redshift universe, providing us with direct observational links to the time shortly after the Dark Ages when the first protogalaxies formed. To date, studies of such stars have largely been restricted to the Milky Way; while our own Galaxy is of course a system of special interest to us, the conclusions that can be drawn from observations of a single object are necessarily limited.

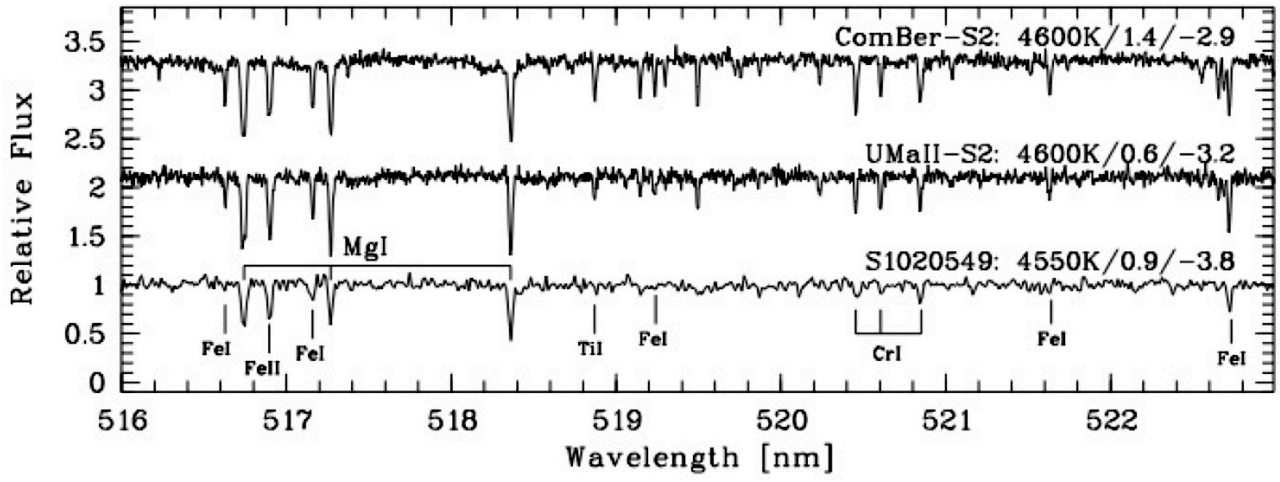

Figure 3-2: Comparison of high-resolution (R ~ 35 K) spectra (around the Mg b triplet lines at 5170 Å) of the Sculptor star S1020549 with [Fe/H] ~ −3.8 with two metal-poor stars ([Fe/H] ~ −3.2 and −2.9) located in the ultra-faint dwarf galaxies Ursa Major II and Coma Berenices (Frebel et al. 2010b). All three stars have similar effective temperatures. Even though S1020549 has a much lower

metallicity than the two other objects, their abundance patterns are nearly identical, suggesting that early chemical evolution may be universal in all galaxies. The total exposure time for S1020549 was 7.55 h; at V = 18.2 this star is among the faintest metal- poor stars observed at high resolution. Because S1020549 is so metal-poor, a high-resolution spectrum with sufficient S/N to measure very weak absorption lines is mandatory. The S/N ratio of the binned spectrum is S/N~22 per 66 mÅ pixel at ~4600 Å and S/N~56 per 133 mÅ pixel at ~6400A. (From Frebel et al., 2010a).

What has prevented extensive observations of old stars in other galaxies is simply a lack of photons. Even the brightest red giants have absolute magnitudes of M_V~ -3, making high S/N, high-resolution spectroscopy with reasonable exposure times possible only for small numbers of stars within ~100 kpc. In Figure 3-3, we show color- magnitude diagrams (CMDs) for a representative set of Milky Way satellite galaxies with distances of up to 250 kpc. With the exception of Sculptor, and perhaps Sextans, a negligible fraction of the stellar population of each galaxy is accessible to detailed abundance studies at present. As a result, rare types of stars -- such as the oldest, lowest-metallicity objects -- are unlikely to be detected. Despite this difficulty, recent surveys have already shown that extremely metal-poor stars down to [Fe/H]~ -3.8, (see Figure 3-2) are plentiful in dwarf galaxies (Frebel, Kirby & Simon 2010; Norris et al. 2010; Tafelmeyer et al. 2010), raising the possibility of investigating the earliest generations of star formation in many independent systems. Future surveys are expected to yield numerous extremely metal-poor stars in these and newly found systems.

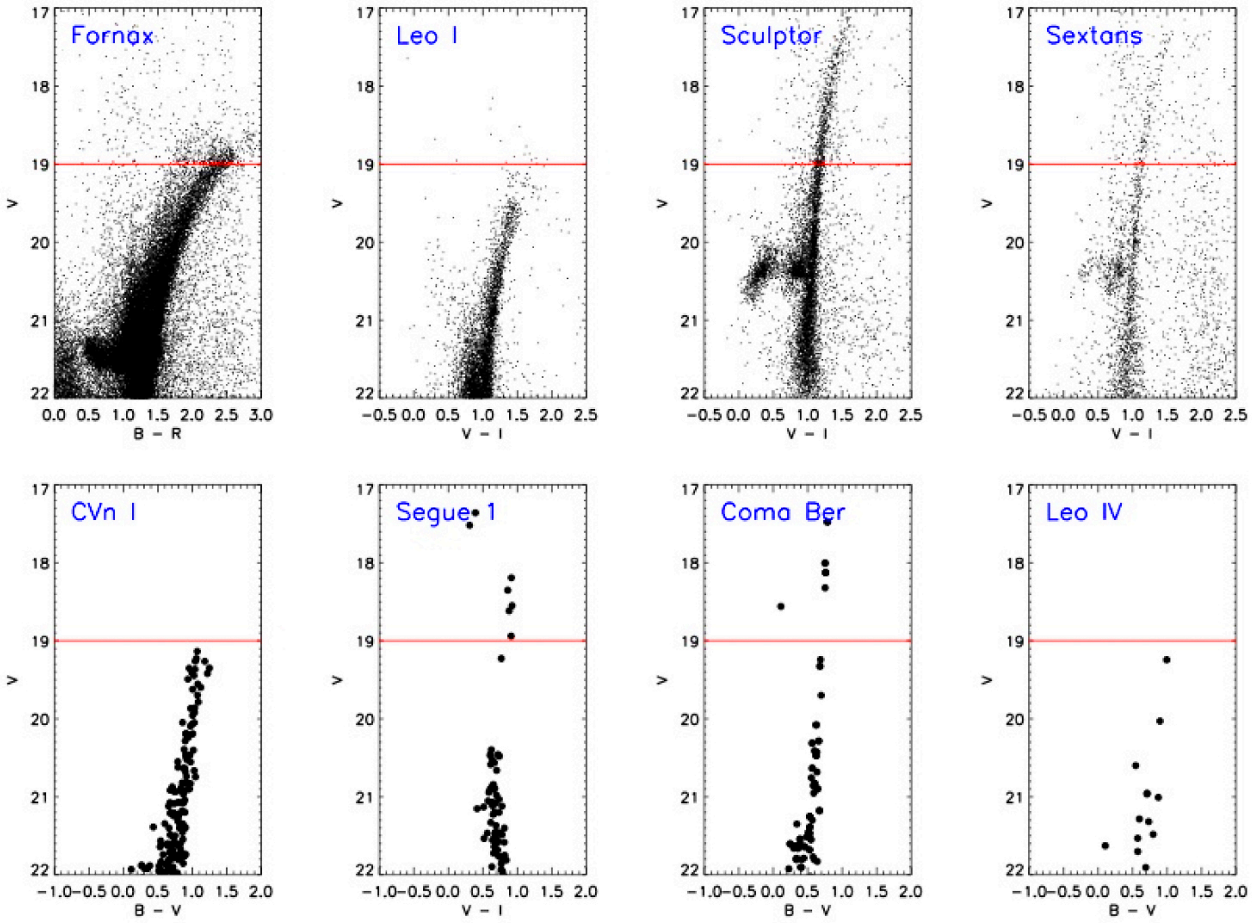

Figure 3-3: Example color-magnitude diagrams of Milky Way satellite galaxies, including classical dwarf spheroidals (upper panels) and ultra-faint dwarfs (lower panels). The red line at V=19 in each CMD illustrates the approximate magnitude limit for high-resolution spectrographs on current telescopes (for ~8 hours of integration). With the exception of Sculptor and Sextans, only a tiny fraction of the population in each galaxy is accessible with current facilities; in the ultra-faint dwarfs the number of stars that can be observed ranges from a handful to none. Fornax data are from Stetson, Hesser, & Smecker-Hane (1998), Leo I data are from Bellazzini et al. (2004), Sculptor data are from Coleman, da Costa, & Bland-Hawthorn et al. (2005), and the other five galaxies are taken from SDSS data.

In the hierarchical assembly of galaxy halos, dwarf galaxies interact gravitationally with their hosts, shedding stars, losing gas, and eventually tidally dissolving into the diffuse halo (Bullock & Johnston 2005). Most dwarf spheroidal galaxies (dSphs) have high mass-to-light ratios, old populations, and very little gas, all of which support the idea that they are stripped remnants that will eventually meld into their host halos, just as their predecessors did. The population of such dwarf

galaxies that exists today may be the lone survivors of the cannibalistic construction of the Galactic halo. Hence, studying dwarf galaxies provides important constraints on this process as well as on the formation and evolution of galaxies less massive than the Milky Way. One of the most interesting questions is: What kind of systems were the "building blocks" of the Milky Way, and what is the relationship of any of the surviving dwarfs to those building blocks?

However, a close inspection of the chemical abundances of individual stars in the "classical" dSphs (e.g. Sculptor, Fornax, Sextans, Carina) obtained over the last decade complicates our understanding of the role of dwarf galaxies in building the Milky Way halo. The abundances suggest that the stellar halo, on average, is not chemically similar to many of its more luminous dSph satellites as would be expected in this picture. In particular, at [Fe/H] > −2, the [α/Fe] ratios are lower in dSph stars than in comparable halo stars (Venn et al. 2004; Tolstoy et al. 2009). Because [α/Fe] indicates the timescale of star formation in a stellar system, it appears that the surviving classical dSphs formed stars for Gyrs longer than the objects that presumably contributed to the Milky Way halo (see Figure 3-4).

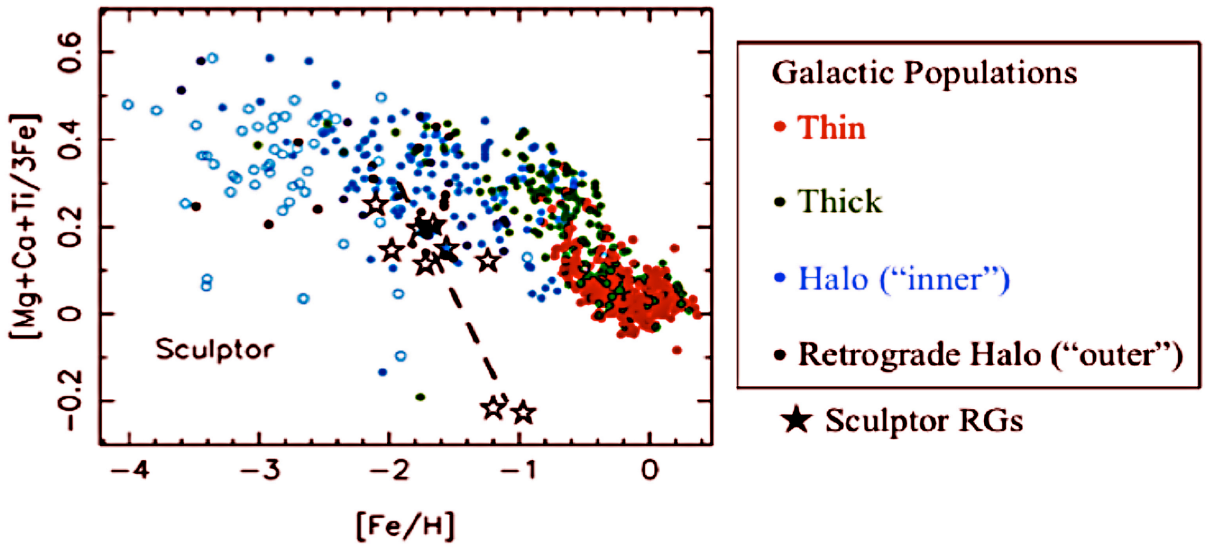

Figure 3-4: α-element abundances for several galactic populations stars compared with Sculptor group red giants. Downturn of α elements abundances at high Z indicates the timescale for chemical evolution in the respective systems.

3.2.1.2. Characterizing the stellar content of dwarf galaxies with G-CLEF

More recent observations of stars in the newly discovered ultra-faint ($L_{tot} \leq 10^5$ $L_\odot$; Martin et al. 2008) dwarf galaxies in SDSS yielded relatively large numbers of extremely metal poor stars in the least luminous systems (Kirby et al. 2008). Their abundance patterns match those of equivalent halo stars (Frebel et al. 2010b; Norris et al. 2010b; Simon et al. 2010; Norris et al. 2010a). This has again opened up the debate whether just the least luminous dwarf galaxies contributed to the most metal-

poor material found in the (primarily outer) stellar halo, and how galaxy formation on the smallest scales may have proceeded. This discussion could be significantly advanced through more observations, but this work is challenging with current facilities. Because the targets are very faint for high-resolution spectroscopy (V>17), one can obtain spectra with adequate S/N (~30-50 at 5000Å) with current 8–10m telescopes to measure detailed chemical abundances only for the very brightest stars in these galaxies down to V~19.2. For the faintest stars, exposure times of 10 hours or more are required (in good sky clarity conditions with 0.7 arcsec seeing), and each individual 1 hour subexposure is at risk of not collecting enough photons to beat down CCD read-noise while not collecting too many cosmic ray hits.

Nevertheless, high-resolution abundance measurements provide many crucial insights into astrophysical questions such as the origin and evolution of the chemical elements, early star and galaxy formation, and the formation of the Galactic halo (and by extension the halos of other galaxies). Some examples are described below.

3.2.1.2.1. Constraints on cosmological simulations of first galaxy formation

The high-redshift origin of surviving ultra faint dwarf galaxies (UFDs) is currently a matter of vigorous debate, with suggestions including H_2-cooling minihaloes (Bovill & Ricotti 2009; Munoz et al. 2009), as well as atomic cooling haloes (Koposov et al. 2009; Li et al. 2010; Maccio et al. 2010). Based on high-resolution spectroscopic abundances of UFD stars, the latter was found to be more plausible in terms of providing viable formation sites for the first Pop II stars. Moreover, these systems may have had only one single Pop III enrichment event that determined the chemical nature of the entire galaxy (Frebel & Bromm 2010). Establishing or disproving these claims with additional abundance data (tens to hundreds of stars rather than just a few stars) for at least some UFDs will provide important constraints on the feedback physics in these early systems and the nature of the first galaxies more generally. These observations will provide an excellent local complement to space-based high-redshift searches for the earliest galaxies with HST and JWST.

3.2.1.2.2. Constraints on Chemical Enrichment in Dwarf Galaxies

Understanding the enrichment processes and chemical evolution in galaxies is of general importance for all of astrophysics. Dwarf galaxies are relatively simple systems (no significant mergers) and thus offer a unique opportunity to study the relevant aspects of their evolution in great detail. As part of that, the observed chemical abundance patterns in dwarf spheroidals (dSphs) can be compared with self-contained star formation models (Lanfranchi & Matteucci 2004; Marcolini et al. 2008). As star formation proceeds, [Fe/H] increases, but after ~1 Gyr, Type Ia supernovae begin to lower [α/Fe]. Therefore, the “knee” in the [α/Fe] vs. [Fe/H] plane indicates the metallicity reached by about 1 Gyr, which in turn indicates the vigor of star formation. Comparing the stellar abundances elements heavier than α-elements, such as Fe-peak or neutron-capture elements (e.g., Sr, Ba, Eu), to supernova yield predictions provides important constraints on supernova and nucleosynthesis physics. Moreover, the top-heavy initial mass function can be probed with the chemical signatures of

the most metal-poor stars in these dwarf galaxies. Such knowledge is crucial for a more complete understanding of the formation mechanisms of small galaxies in the early Universe.

3.2.1.2.3. Constraints on the formation of the Galactic Halo

In the coming decade, synergy between model predictions and observations will advance our understanding of the formation of the Milky Way halo. It is difficult to directly observe the progenitor systems of the bulk of the halo because they have already been destroyed. However, it is possible to connect the properties of surviving dSphs and stellar halos using models of galactic star formation and chemical enrichment. These simulations make predictions about the kinematics (Helmi et al. 1999; Font et al. 2006b) and chemistry (Font et al. 2006a) of the relics of accretion events. Testing these predictions will require coordinated spectroscopic surveys focused on measuring as many chemical abundances and radial velocities as possible for a large number of stars in different types of dwarf galaxies. Measurements of different abundance groups such as α-elements, neutron-capture elements, and carbon will provide important constraints on the production mechanisms and their specific environments in the early universe. This will ultimately shed light on the origin of the halo star abundance patterns (many of which are unexplained at present; e.g., the large number of carbon-enhanced EMP stars) and thus offer a more differentiated view of what the cosmological origin of the most metal-poor halo stars are. This, in turn, will support or challenge the theory of the hierarchical assembly of galaxies.

3.2.2. Science Requirements (Level 1 Requirements)

A resolution of R~20,000 is the minimum required for these observations of suitable wavelength chunks that contain important elemental absorption lines to study the chemical abundance patterns. The targets will naturally be faint (V = 18−20), but G-CLEF can observe V=20 targets in ~2h with R=20,000 (in single objects mode, assuming 0.7 arcsecond seeing, an average airmass of 1.5 and lunar phase=7, as well as 7 mirrors; see Table 3-4). V=21.5 targets would require ~30h per pointing, so multiobject capability will enable statistically significant samples in most galaxies. This will be particularly important for the numerous new dwarf galaxies expected to be discovered in current and planned surveys (e.g., the southern Skymapper, LSST).

G Mag	Res.	S/N	λ	T_{exp} (4 Mirrors)	T_{exp} (7 Mirrors)
20	20K	30	5000Å	3.5 hours	2 hours
21.5	20K	30	5000Å	50 hours	27 hours

Table 3-4: Exposure times for single-star high resolution dwarf galaxy spectra for 4 and 7 mirrors in 0.7 arcsec seeing.

However, single-star observations without multiobject spectroscopy capability provided by MANIFEST will also already yield important science results as recent dwarf galaxy studies have demonstrated (e.g. Frebel et al. 2010). Even a sample of 10 stars in 5 dwarf galaxy stars down to 20

mag would take ~10 nights. This would allow one to probe the base of the red giant branch, which is currently impossible.

Table 3-5: Operational requirements for dwarf galaxy observing program.

3.2.3. References

Bellazzini, M., Gennari, N., Ferraro, F. R., & Sollima, A. 2004, *The distance to the Leo I dwarf spheroidal galaxy from the red giant branch tip*, MNRAS, 354, 708.

Bovill, M. S. & Ricotti, M. 2009, *Pre-Reionization Fossils, Ultra-Faint Dwarfs, and the Missing Galactic Satellite Problem*, ApJ, 693, 1859

Bullock, J. S., & Johnston, K. V. 2005, *Tracing Galaxy Formation with Stellar Halos. I. Methods*, ApJ, 635, 931

Cayrel, R., et al. 2004, *First stars V - Abundance patterns from C to Zn and supernova yields in the early Galaxy*, A&A, 416, 1117

Coleman, M. G., Da Costa, G. S., & Bland-Hawthorn, J. 2005, *The Absence of Extratidal Structure in the Sculptor Dwarf Spheroidal Galaxy*, AJ, 130, 1065

Font, A. S., et al. 2006a, *Chemical Abundance Distributions of Galactic Halos and Their Satellite Systems in a ΛCDM Universe*, ApJ, 638, 585

Font, A. S., et al. 2006b, *Phase-Space Distributions of Chemical Abundances in Milky Way-Type Galaxy Halos*, ApJ, 646, 886

Frebel, A. 2010, *Stellar archaeology: Exploring the Universe with metal-poor stars,* Astronomische Nachrichten, 331, 474

Frebel, A. & Bromm, V. 2012, *Chemical Signatures of the First Galaxies: Criteria for One-shot Enrichment*, ApJ 759, 115

Koch, A. 2009, *Complexity in small-scale dwarf spheroidal galaxies (Ludwig Biermann Award Lecture 2008)*, Astronomische Nachrichten, 330, 675

Koposov, S. E. et al. 2009, *A Quantitative Explanation of the Observed Population of Milky Way Satellite Galaxies,* ApJ, 696, 2179

Lanfranchi, G. A., & Matteucci, F. 2004, *The predicted metallicity distribution of stars in dwarf spheroidal galaxies,* MNRAS, 351, 1338

Li, Y., De Lucia, G., & Helmi, A. 2010, *On the nature of the Milky Way satellites*, MNRAS, 401, 2036

Macciò, A. V. et al. 2010, *Luminosity function and radial distribution of Milky Way satellites in a ΛCDM Universe,* MNRAS, 402, 1995

Marcolini, A., et al. 2008, *The chemical evolution of dwarf spheroidal galaxies: dissecting the inner regions and their stellar populations*, MNRAS, 386, 2173

Martin, N. F., de Jong, J. T. A., & Rix, H.-W. 2008, *A Comprehensive Maximum Likelihood Analysis of the Structural Properties of Faint Milky Way Satellites*, ApJ, 684, 1075

Munoz, J. A., Madau, P., Loeb, A., & Diemand, J. 2009, *Probing the epoch of reionization with Milky Way satellites,* MNRAS, 400, 1593

Norris, J. E., Gilmore, G., Wyse, R. F. G., Yong, D., & Frebel, A. 2010, *An Extremely Carbon-rich, Extremely Metal-poor Star in the Segue 1 System,* ApJ, 722, L104

Norris, J. E., Yong, D., Gilmore, G., & Wyse, R. F. G. 2010b, *Boo-1137—an Extremely Metal-Poor Star in the Ultra-Faint Dwarf Spheroidal Galaxy Boötes I*, ApJ, 711, 350

Simon, J. D., Frebel, A., McWilliam, A., Kirby, E. N. & Thompson, I. B. 2010, *High-resolution Spectroscopy of Extremely Metal-poor Stars in the Least Evolved Galaxies: Leo IV*, ApJ, 716, 446

Spite, M., & Spite, F. 1982, *Lithium abundance at the formation of the Galaxy,* Nature, 297, 483

Stetson, P. B., Hesser, J. E., & Smecker-Hane, T. A. 1998, *Homogeneous Photometry for Star Clusters and Resolved Galaxies. I. A Survey of Bright Stars in the Fornax Dwarf Spheroidal Galaxy,* PASP, 110, 533

Tafelmeyer, M., et al. 2010*, Extremely metal-poor stars in classical dwarf spheroidal galaxies: Fornax, Sculptor, and Sextans,* A&A, 524, A58

Tolstoy, E., Hill, V., & Tosi, M. 2009, *Star-Formation Histories, Abundances, and Kinematics of Dwarf Galaxies in the Local Group*, AR&AA, 47, 371

Tyson, J. A. 2002, *Large Synoptic Survey Telescope: Overview*, Proceedings of SPIE, 4836, 10

Venn, K. A., Irwin, M., Shetrone, M. D., Tout, C. A., Hill, V., & Tolstoy, E. 2004*, Stellar Chemical Signatures and Hierarchical Galaxy Formation,* AJ, 128, 1177

4. Cosmology Studies

4.1. Probing the Cosmic Dawn

4.1.1. Science Drivers (Level 0 Requirements)

4.1.1.1. Introduction

The formation of the first luminous sources marks the start of a fundamental transition in the physical state of the early Universe. These first stars and galaxies produced ultraviolet radiation and heavy elements which reionized and chemically enriched the primordial material from which they were born. This cosmic dawn epoch lies at the frontier of modern observational astronomy and is one of the top priorities in astrophysical research in the forthcoming decade. Studies of the intergalactic medium (IGM) traced by absorption in the spectra of quasars and gamma-ray bursts (GRBs) at $z \geq 5$ provide one of the key observational probes of the cosmic dawn and epoch of reionization (Fan et al., 2006, Totani et al., 2006, Mortlock, et al., 2011). Detailed studies of intergalactic absorption lines enable constraints on the ionization state of the IGM in the early Universe (Mesinger & Haiman, 2004, Mc Greer, Mesinger & Fan, 2011, Bolton, et al., 2011), as well as measurements of related quantities such as the IGM temperature (Becker, et al., 2011, Theuns, et al., 2002) and the abundances of heavy elements (Ryan-Weber et al., 2009, Simcoe, et al., 2011). These data thus contain valuable information on the reionization process that are inaccessible with other, complementary observational probes of the high redshift Universe.

Existing spectra of the brightest known quasars at $z \approx 6$ ($z_{AB} \sim 19.5$) typically have moderate resolution ($R \sim 3000 - 6000$) and/or S/N~ 20, even when using the largest of the current generation of optical telescopes (Fan, et al., 2006). Moreover, these spectra are attainable from a subset of known $z \sim 6$ quasars only. This lends these data limited power for distinguishing among differing reionization histories due to cosmic variance uncertainties arising from the inhomogeneous nature of the intervening IGM density and ionization state (Mesinger, 2010). A handful of high resolution spectra ($R \sim 40000$) at $z > 6$ have also been attained at moderate S/N~ 10−20 for the very brightest quasars, although these typically require exposure times of $t_{exp} > 8$ hrs with an $8 - 10$ m class telescope (Calverley, et al., 2011). The improvement in sensitivity provided by the GMT, combined with high resolution optical spectroscopy with G- CLEF, will thus provide the capability to probe the IGM toward the tail-end of the cosmic dawn era from $z \approx 5 - 6.8$ with high spectral resolution and superior S/N. Furthermore, larger data sets will also be possible with access (at lower S/N) to high resolution data for fainter background quasars ($z_{AB} \sim 21.0$, e.g. Willott, et al., 2010), and possibly GRBs, resulting in a commensurate improvement in the statistical power of the data. This aspect is vital for probing reionization in detail, since it is an inherently spatially and temporally inhomogeneous process.

4.1.1.2. Detecting high-redshifted Lyman-alpha absorption in z=6-7 quasars: High resolution constraints on the IGM ionization state

As a quantitative example, Fig. 1 displays a numerical simulation of intergalactic Lyα absorption in the spectrum of a z = 6.30 quasar. The upper panel displays the quasar spectrum at a spectral resolution (R ~ 3000) and S/N= 20 per pixel similar to data obtained with an exposure time, t_{exp} = 1 hr, with Keck/ESI on the brightest (z_{AB} ~ 19.5) known quasars at high redshift (Fan et al., 2006). The lower panel displays the same spectrum with a resolution and S/N representative of future data obtained with GMT/G-CLEF (R ~ 40000) and t_{exp} = 4 hr. The greater wealth of information available at high spectral resolution enables detailed insight into reionization the physical state of the IGM, facilitating tighter constraints on the ionization state of the IGM and the measurement of the temperature evolution of the IGM.

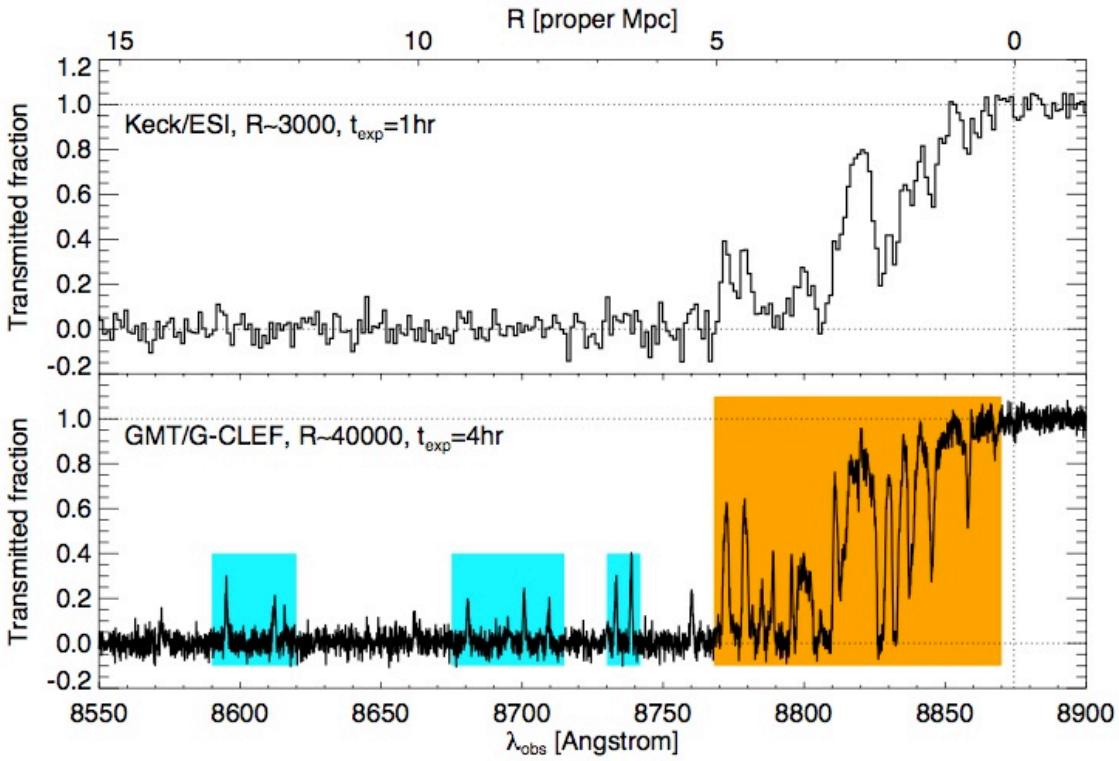

Figure 4-1: Simulated spectrum of a quasar at z = 6.30 displaying transmission blueward of the Lyα transition in the quasar rest frame (λ_{obs} = 8874.4A, vertical dotted line). The spectrum is constructed using a cosmological hydrodynamical structure formation simulation combined with a line of sight radiative transfer model for the quasar ionizing radiation field. The transmitted fraction is plotted against observed wavelength (lower horizontal axis) and proper distance from the quasar (upper horizontal axis) following normalization of the spectrum by the intrinsic quasar emission. Upper

panel: Spectrum with noise and resolution characteristics similar to data obtained with Keck/ESI for the brightest known quasars (z_{AB}~19.5) at z ≃ 6 with an exposure time of one hour. The spectral resolution is R = 3000 with a S/N~20 per pixel. Lower panel: The same quasar, but at a spectral resolution of R = 40 000 and S/N~27 per pixel following a four hour exposure with GMT/G- CLEF. The intrinsic widths of Lyα absorption lines in the quasar "near-zone" (orange shading) are now fully resolved, while narrow transmission peaks in the Gunn-Peterson trough (cyan shading) are unambiguously detected, indicating patches of highly ionized IGM along this particular line-of-sight.

Analyses of the size and shape of the Lyα transmission in the highly ionized near-zone of the quasar (Fig. 1, orange shading) and the statistics of dark gaps and Lyα transmission peaks along the line-of-sight (Fig. 1, cyan shading) may be used to constrain the IGM ionization state. Near-zones are potentially sensitive to volume weighted neutral hydrogen fractions surrounding the quasar of $\langle f_{HI} \rangle \sim 0.1 - 1$, providing a marked improvement on the lower limit of $\langle f_{HI} \rangle \sim 10^{-4}$ achievable with the well known Gunn-Peterson optical depth constraint. (More stringent constraints on $\langle f_{HI} \rangle$ are impossible using the Gunn-Peterson optical depth alone due to the small neutral hydrogen fractions at which Lyman series absorption saturates.) These highly ionized near-zones arise because of the enhanced ionization state of the IGM around these luminous sources. When the edge of the near-zone traces the position of the H II ionization front propagating outwards from the quasar, the relative extent of near-zones observed in Ly α and Ly β absorption is sensitive to an HI fraction around the quasar with $\langle f_{HI} \rangle > 0.1$. However, several tens of spectra are required to average over the large scatter in individual line-of-sight measurements arising from cosmic variance, and high resolution, high S/N data increases the reliability of the measurement (Bolton & Haehnelt, 2007).

The overall shape of the Lyα transmission in the quasar near-zone is also well resolved at high resolution and S/N. This can be used to identify the possible "damping-wing" signature of neutral gas along the quasar or GRB sight-line, which arises from the red Lorentzian wing of the resultant Gunn-Peterson trough. There is now evidence that such a damping wing is present in the spectrum of the highest redshift quasar yet discovered at z = 7.08 (Bolton, et al., 2011, Mortlock et al., 2011). However, the interpretation of this damping wing is complicated if a proximate or intrinsic collapsed system with high H I column density also produces a damping wing (Miralda-Escude, 1998, McQuinn, 2008). The ability to distinguish between the shape of a damping wing caused by an extended neutral medium (which declines as $[\lambda_{obs}/\Delta\lambda_{obs}]$) or a discrete collapsed system (which declines as $[\lambda_{obs}/\Delta\lambda_{obs}]^2$ will be assisted by the high resolution and S/N spectra afforded by G-CLEF.

The fraction of dark gaps in absorption spectra may also be used to constrain the IGM neutral fraction at z > 5. Narrow features indicating highly ionized patches along the line-of-sight, which are difficult to detect in the trough of absorption in the lower resolution spectrum, are clearly apparent in the simulated G-CLEF spectrum (Fig. 1, cyan shading). The statistics of these regions may be used to place model independent upper limits on the IGM neutral fraction (McGreer, et al. 2011).

Crucially, higher resolution data can resolve these transmission peaks on small scales and place tighter constraints on the H I fraction.

4.1.1.3. Characterizing the thermal evolution of the IGM following reionization with G-CLEF

Finally, the high spectral resolution afforded by G-CLEF also facilitates the measurement of the intrinsic widths of Lyα absorption features in the quasar near-zone (Fig. 1, orange shading). Resolving the relatively narrow thermal widths of these lines, $b = 12.9 \text{ km s}^{-1}(T/10^4 \text{ K})^{1/2}$, requires high resolution (R ~ 40 000) spectroscopy. This enables the temperature of the gas in the near zones to be directly measured. Intergalactic hydrogen is predominantly photo-heated by ultraviolet radiation, and is thus sensitive to prior photo-heating by sources of ionizing photons. Since the cooling time scale in the low-density IGM is long (Hui & Haiman, 2003, Theuns, et al., 2002), information on the reionization history and any subsequent heating by the quasar is encoded in the thermal widths of these absorption lines. Furthermore, the amount of photo-heating is dependent on the ionizing spectrum; a hard ionizing spectrum (e.g. metal-free stars) will result in a larger IGM temperature immediately following the reionization of hydrogen. Initial attempts at this measurement using high resolution, moderateto S/N~ 20 Keck/HIRES spectra at z ≃ 6 suggests this approach has promise (Bolton, et al., 2012); larger data sets and higher signal-to-noise will be in reach with GMT/G-CLEF. The ability of the G-CLEF to obtain such high quality data will provide a valuable step forward in our understanding of the physical state of the IGM approaching the cosmic dawn epoch at z > 5.

4.1.2. Science Requirements (Level 1 Requirements)

Quasars with magnitudes of z_{AB}=19.5 (bright) and z_{AB}=21.0 (faint) are broadly representative of current z~6-7 quasars (see e.g., Fan et al., 2006, Willott et al., 2010). Measuring the redshifted Lyman-alpha line at λ_r=1216A then in the 7900Å->9500Å regime is the prime goal.

Assuming a seeing of 0.7 arcsec (less than 1 arcsec required), a lunar phase of within 5-7 days of new moon and R~40,000, it takes up to 56h with 7 mirrors to observe a fainter quasar to reach a S/N=30 (see Table 4-1). This exposure time could be reduced by accepting a S/N~20, which is the bare minimum. These requirements, however, make it impossible to use a 4 mirror GMT for the higher redshift (i.e. fainter) quasars, as can also be seen in the Table 4-1.

z Mag	Resolution	S/N	λ	T_{exp} (4 mirrors)	T_{exp} (7 mirrors)
19.5	40K	30	8700 Å	8 Hours	4.4 Hours
21	40K	30	8700 Å	98 Hours	56 Hours

Table 4-1: Exposure times for high resolution quasar spectra for 4 and 7 mirror GMTs.

4.1.3. References

G. D. Becker, J. S. Bolton, M. G. Haehnelt, and W. L. W. Sargent, 2011, *Detection of extended He II reionization in the temperature evolution of the intergalactic medium,* MNRAS, 410, 1096.

J. S. Bolton, G. D. Becker, S. Raskutti, J. S. B. Wyithe, M. G. Haehnelt, and W. L. W. Sargent, 2012, *Improved measurements of the intergalactic medium temperature around quasars: possible evidence for the initial stages of He II reionization at z ~ 6,* MNRAS, 419, 2880.

J. S. Bolton and M. G. Haehnelt, 2007, *A closer look at using quasar near-zones as a probe of neutral hydrogen in the intergalactic medium,* MNRAS, 381, L35.

J. S. Bolton, M. G. Haehnelt, S. J. Warren, P. C. Hewett, D. J. Mortlock, B. P. Venemans, R. G. McMahon, and C. Simpson, 2011, *How neutral is the intergalactic medium surrounding the redshift z = 7.085 quasar ULAS J1120+0641?,* MNRAS, 416, L70.

A. P. Calverley, G. D. Becker, M. G. Haehnelt, and J. S. Bolton, 2011, *Measurements of the ultraviolet background at 4.6 < z < 6.4 using the quasar proximity effect,* MNRAS, 412, 2543.

X. Fan, M. A. Strauss, R. H. Becker, R. L. White, J. E. Gunn, G. R. Knapp, G. T. Richards, D. P. Schneider, J. Brinkmann, and M. Fukugita, 2006, *Constraining the Evolution of the Ionizing Background and the Epoch of Reionization with z ~ 6 Quasars. II. A Sample of 19 Quasars*, AJ, 132, 117.

L. Hui and Z. Haiman, 2003, *The Thermal Memory of Reionization History*. ApJ, 596, 9.

I. D. McGreer, A. Mesinger, and X. Fan, 2011, *The first (nearly) model-independent constraint on the neutral hydrogen fraction at z ~ 6.* MNRAS, 415, 3237.

M. McQuinn, A. Lidz, M. Zaldarriaga, L. Hernquist, and S. Dutta, 2010, *Probing the neutral fraction of the IGM with GRBs during the epoch of reionization,* MNRAS, 388, 1101.

A. Mesinger, 2010, *Was reionization complete by z ~ 5–6?,* MNRAS, 407, 1328.

A. Mesinger and Z. Haiman. *Evidence of a Cosmological Strömgren Surface and of Significant Neutral Hydrogen Surrounding the Quasar SDSS J1030+0524,* 2004, ApJ, 611, L69.

J. Miralda-Escude, 1998, *Reionization of the Intergalactic Medium and the Damping Wing of the Gunn-Peterson Trough.* ApJ, 501, 15.

D. J. Mortlock, S. J. Warren, B. P. Venemans, M. Patel, P. C. Hewett, R. G. McMahon, C. Simpson, T. Theuns, E. A. Gonzáles-Solares, A. Adamson, S. Dye, N. C. Hambly, P. Hirst, M. J. Irwin, E.

Kuiper, A. Lawrence, and H. J. A. Röttgering, 2011, *A luminous quasar at a redshift of z = 7.085.* Nature, 474, 616.

E. V. Ryan-Weber, M. Pettini, P. Madau, and B. J. Zych, 2009, *A downturn in intergalactic CIV as redshift 6 is approached.* MNRAS, 395, 1476.

R. A. Simcoe, K. L. Cooksey, M. Matejek, A. J. Burgasser, J. Bochanski, E. Lovegrove, R. A. Bernstein, J. L. Pipher, W. J. Forrest, C. McMurtry, X. Fan, and J. O'Meara, 2011, *Constraints on the Universal C IV Mass Density at z ~ 6 from Early Infrared Spectra Obtained with the Magellan FIRE Spectrograph.* ApJ, 743, 21.

T. Theuns, J. Schaye, S. Zaroubi, T.-S. Kim, P. Tzanavaris, and B. Carswell, 2002, *Constraints on Reionization from the Thermal History of the Intergalactic Medium.* ApJ, 567, L103.

T. Totani, N. Kawai, G. Kosugi, K. Aoki, T. Yamada, M. Iye, K. Ohta, and T. Hattori. 2006, *Implications for Cosmic Reionization from the Optical Afterglow Spectrum of the Gamma- Ray Burst 050904 at z = 6.3.* PASJ, 58, 485.

C. J. Willott, P. Delorme, C. Reylé, L. Albert, J. Bergeron, D. Crampton, X. Delfosse, T. Forveille, J. B. Hutchings, R. J. McLure, A. Omont, and D. Schade. 2010, *The Canada-France High-z Quasar Survey: Nine New Quasars and the Luminosity Function at Redshift 6*. AJ, 139, 906.

4.2. A Search for Variations in Fundamental Constants Over Cosmological Time Scales?

4.2.1. Science Drivers (Level 0 Requirements)

- Determine the constancy of the fine structure constant (α) over cosmic time.

4.2.1.1. Introduction

The Standard Model of particle physics is arguably humanity's most successful theory. Its predictions are regularly tested to exquisite precision in laboratories around the world and, so far, experiment continues to agrees with theory. But at its most fundamental level the Standard Model seems incomplete: it is parameterized by several dimensionless "fundamental constants", such as coupling constants and mass ratios, whose values are not predicted by the Model itself. Nor can the Standard Model say anything about their constancy – that must also be established by experiment. Our confidence in their constancy stems from Earth-bound laboratory experiments conducted over human time scales (e.g. Rosenband et al. 2008). But dramatic variations might have occurred over the 13–14 billion-year history of the Universe and the residual variations might remain undetectably small in the tiny corner of space-time in which we conduct experiments. Indeed, in some 'beyond-Standard' theoretical models, particularly those seeking to unify the four forces of nature (e.g. String/M-theory), the 'constants' vary naturally on cosmological time- and distance-scales (see Uzan

2003 for a review). It is therefore imperative to measure the constants in widely separated regions of the distant Universe and throughout its history.

One such parameter whose constancy can be tested to high precision is the fine-structure constant, $\alpha \equiv e^2/\hbar c$, which characterizes electromagnetism's strength. Variations in α would manifest themselves as shifts in the transition energies of atoms. By comparing laboratory transition energies with the values registered in spectra of astronomical objects, possible variations can be probed, in principle, over our entire observable Universe and throughout most of its history. If α were found to vary in space-time, understanding its dynamics would require a more fundamental theory, perhaps one unifying the four known physical interactions. Conversely, observational constraints on its variability may rule out certain classes of such "theories of everything".

4.2.1.2. Current status

The most precise cosmological probes in this context are absorption lines arising in gas clouds which happen to intersect the sight-lines to bright background quasars. Uzan (2003) summarizes the early null results. The last decade has seen some evidence for cosmological variations in α emerge from absorption-line studies. A crucial step was an order of magnitude sensitivity gain from comparing transitions from many multiplets of different metallic ions (Dzuba et al. 1999) – see Figure 5.8.

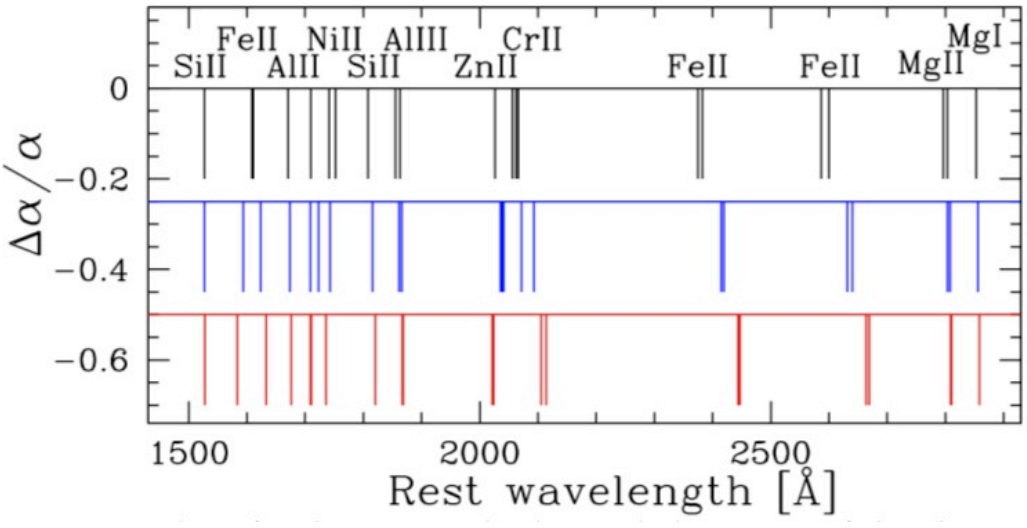

Table 4-2: Dependence of metal transition wavelengths on α. The distinct pattern of relative line shifts (i.e. velocity shifts between transitions) is encoded into the quasar absorption spectra.

Whereas previous studies focused on doublets of alkali-like ions, Webb et al. (1999) used this "many multiplet" method to compare 8 transitions of MgII and FeII in 14 quasars from the 10-meter Keck telescope. They constrained α to an unprecedented relative precision of a few parts per million (ppm) for the ensemble and found tentative evidence for a smaller α in absorption clouds at redshifts z =

0.5–1.6 relative to the current laboratory value. With an independent Keck dataset, Murphy et al. (2001a) strengthened this low-z evidence, extended it to higher redshift and used many more transitions further into the rest-frame ultraviolet (see Figure 5.8). The Keck evidence for a smaller α in distant galaxies now stems from three independent datasets containing 143 absorbers covering redshifts z = 0.2–4.2 and is statistically quite strong (Murphy et al. 2003; Murphy et al. 2004): $\Delta\alpha/\alpha = (-5.7 \pm 1.1)$ ppm, where $\Delta\alpha/\alpha$ is the relative deviation from the current laboratory value of α. Moreover, despite much scrutiny of potential astrophysical and instrumental systematic errors, no "mundane" explanation of these results has been found (e.g. Murphy et al. 2001b; Murphy et al. 2003; Bahcall et al. 2004; Murphy et al. 2004; Murphy et al. 2009; Griest et al. 2010; Whitmore et al. 2010).

A further observational twist has recently emerged: some evidence for spatial variations in α across the sky exists in the only large VLT/UVES sample to date, 153 absorbers studied by Webb et al. (2011), see also King et al., 2012. And when the predominantly southern observations of the new VLT sample are combined with the more northern Keck sample, ~4σ evidence for a dipole-like variation in α across the sky is found.

Efforts to refine these measurements continue, but they are united by an important weakness: they rely on quasar spectra obtained with fairly unstable slit spectrographs and are calibrated using separately-observed arc lamp exposures. The fundamental physical question at hand demands much more accurate and robust wavelength calibration of quasar spectra. And if the spatial variation claims are to be confidently ruled out (or confirmed!), a statistically meaningful sample, spread over (some of) the sky, is required together with much tighter constraints on α-variation in individual absorption systems.

4.2.2. Science Requirements (Level 1 Requirements)

Addressing the three main challenges specified above requires a sample of at least ~20 QSOs, spread over reasonable redshift, RA and Dec. ranges, with each absorber providing a statistical precision of ⩽1ppm per absorber. The statistical precision achievable on α-variation is driven mainly by the spectral S/N. The S/N requirement for the above G-CLEF program can be estimated by comparison with the large Keck and VLT absorber samples of Murphy et al. (2004) and King et al. (2012). There, an absorber with a typical number of "many multiplet" transitions (~7) from Figure 5.8 and a S/N of ~30 per 2.5 km/s pixel yielded typical statistical errors of ~10 ppm on $\Delta\alpha/\alpha$. Assuming we can use a similar number of transitions per absorber in a G-CLEF spectrum, and using the HR mode with 1 km/s pixels, the S/N required is $30 \times 10\text{ppm}/1\text{ppm} \times 1/\sqrt{2.5} = 188$ per 1 km/sec pixel. This is an upper limit because, in practice, some relatively unblended "clouds" will exist in some absorbers and so the higher resolution of the G-CLEF observations (R=100 k vs. ~50-60 k for Keck or VLT) will increase the precision on $\Delta\alpha/\alpha$.

The Keck and VLT absorber samples of Murphy et al. (2004) and King et al. (2012) also allow a rough prediction of how many bright QSOs contain at least one "useful" absorption system, i.e. one

where at least ~7 of the transitions shown in Figure 5.8 strongly absorb the continuum (to optical depth > 0.5). A conservative estimate is that ~30 southern QSOs brighter than mag (AB; r-band)=17.0 contain 2 or more such absorbers. The G-CLEF ETC reports that with this AB magnitude, a 3000s exposure provides S/N=32 per 1-km/s pixel in HR mode with default settings (airmass=1.2, lunar phase=7 days, seeing=0.7 arcsec). Assuming a 5-min overhead per exposure, achieving a S/N of 212 would therefore require ~35 hours per QSO. With ~20 QSOs this amounts to ~700 hours, or ~70 nights. Some QSOs will be brighter and less time can be spent on them. Since observing as "faint" as 17.0 mag allows for selecting QSOs with $\geqslant$2 high quality absorbers per sight-line, this will yield $\geqslant$40 $\Delta\alpha/\alpha$ measurements with a minimum statistical precision of 1ppm per absorber, i.e. an ensemble precision of ~0.16 ppm. This is unprecedented "precision fundamental physics" in the distant Universe. Spread over the sky, these measurements will strongly rule out – or confirm – the current evidence (or any near-future incremental improvement in it) for time and/or spatial variations in α.

Target	N_{Obj}	Resol.	S/N	t_{Exp}	Goal Result
QSO with z ⩾ 2 absorpt.systems	20	100,000	212	35 Hours	Many-multiplet determination of constancy of α

Table 4-3: Observational requirements for many-multiplet search for variation of α.

References:

Bahcall J.N., Steinhardt C.L. & Schlegel D., 2004, ApJ, 600, 520.

Dzuba V.A., Flambaum V.V. & Webb J.K., 1999, Phys. Rev. Lett., 82, 888.

Griest K., Whitmore J.B., Wolfe A.M., Prochaska J.X., Howk J.C., Marcy G.W., 2010, ApJ, 708, 158.

King J.A., Webb J.K., Murphy M.T., Flambaum V.V., Carswell R.F., Bainbridge M.B., Wilczynska M.R., Koch F.E., 2012, MNRAS, 422, 3370.

Murphy M.T., Webb J.K, Flambaum V.V., Dzuba V.A., Churchill C.W., Prochaska J.X., Barrow J.D. & Wolfe A.M., 2001a, MNRAS, 327, 1208.

Molaro P., Reimers D., Agafonova I.I. & Levshakov S.A., 2008, Euro. Phys. J. Special Topics, 163. 173.

Murphy M.T., Webb J.K, Flambaum V.V., Churchill C.W. & Prochaska J.X., 2001b, MNRAS, 327, 1223.

Murphy M.T., Webb J.K, Flambaum V.V., Dzuba V.A., Prochaska J.X. & Wolfe A.M., 2004, Lecture Notes in Physics, 648, 131.

Murphy M.T., Tzanavaris P., Webb J.K. & Lovis C., 2007a, MNRAS, 378, 211.

Murphy M.T. et al., 2007b, MNRAS, 380, 839.

Murphy M.T., Webb J.K. & Flambaum V.V., 2009, Mem. della Soc. Astron. Italiana, 80, 833. Rosenband T. et al., 2008, Science, 391, 1808.

Uzan J-P. et al, 2003, Rev. Mod. Phys., 75, 403.

Webb J.K., Flambaum V.V., Churchill C.W., Drinkwater M.J. & Barrow J.D., 1999, Phys. Rev. Lett., 82, 884.

Webb J.K., King J.A., Murphy M.T., Flambaum V.V., Carswell R.F. & Bainbridge M.B., 2011, Phys. Rev. Lett., 107, 191101

Wilken T., Lovis C., Manescau A., Steinmetz T., Pasquini L., Lo Curto G., Hänsch T.W., Holzwarth R. & Udem Th., 2010, MNRAS, 405, 16L.

Whitmore J.B., Murphy M.T. & Griest K., ApJ, 2010, 723, 89.

5. Requirements Summary

5.1. Summary Level 3 Requirements

We summarize the Science (Level 1) Requirements in Table 5-1. We note several of them will be subject to revision between now and Instrument Requirements Review. The throughout requirement appear in this table for the first time for the following reason. During the CoD study, we wrote an prototype exposure time calculator (PETC) that all authors of the CoD and SRR document to develop science cases for G-CLEF. The predicted G-CLEF throughput was embedded in the PETC code. It is somewhat difficult to deconvolve the relationships between the various input parameters to the PETC in generating the science cases (moon phase, air mass, seeing, adopted model spectra, etc.). However the throughput model in the PETC is the basis for all quantitative predictions of G-CLEF scientific performance. For this reason, we simply draw requirement values directly from the PETC itself.

A second issue is that of alignment of G-CLEF science requirements and those of the GMT. We note that at the time of G-CLEF SRR, the GMT Science Requirements are still at GMT Board review. We expect the SRR itself will be a forum to discuss aligning the two sets of requirements. We do offer the compliance matrix from the CoDR proposal, that demonstrated compliance with the requirements in the calls for proposal for both the Precision Radial Velocity Spectrograph (PRVS) and the High Resolution Visible Spectrograph concepts. This matrix is included as Appendix A.

#	Requirement	Value		Comments
3.1.1 & 4.1.1	Passband	3500Å-1μ		
2.1.2, 3.1.2, 3.2.2	Resolution	20k, 40k & 100k		
2.1.3 & 4.2.3	Slicing	Yes		Pupil & Image
All	Thoughput	3500Å	3%/PA	
		5000Å	7%/PRV	
		7000Å	12% HT	
		8000Å	7%/PRV	
		1μ	1%/HR	
2.2.4	Bright Limit	$M_R < 6$ must be observable		Includes guide and AO
All	CCD Type	Blue & Red Enhanced		
2.2.6	CCD Linear Regime	36,000		
2.2.7/3.2.4	CCD Readout	Fast/Slow		
2.2.8/3.2.4	CCD RON	5		
All	Operating Air Mass	⩽2		
Most/4.1.8	Telescope Aperture	4 or 7 Mirror/7 Mirror		Early science w/ 4 mirrors
All	AO	Desirable		
2.1.13, 2.2.14, 4.1.9	Operational	Flexible, rapid queuing required		
2.1.15	Single Meas. RV	40-50 cm/sec		TBR
3.2.4 & 3.3.4	MOS	Required		

Table 5-1: Summary science requirements table for G-CLEF.

Appendix A: The G-CLEF CoD Proposal Compliance Matrix.

Element	Spec	Goal	G-CLEF	PRVS?	HRVS?	Notes
Passband	4000-9500Å	3200Å-1.1μ	3500-9500Å		√	
	4000-7000Å	3200-8500Å		√		
Resolution (Rϕ)	≥30,000		20,000 40,000 100,000 & 150,000		√	Resolutions achieved with different operating modes.
	100,00			√		
Image Quality	<0.25”	<0.15”	n/a			
Slit Length	≥3”					
Velocity Precision	≤100 m/s		√		√	
	≤ 1m/s	≤ 20 cm/sec	TBD			
Throughput	≥20%	≥30%	√		√	4000-9000Å
Band-limiting Filters			√		Req.	
Internal Calibration			√		Req.	
ADC			√		Opt.	
Derotation					Opt.	
Fiber Input			√		Opt.	
Wavelength Reference Std.			√	√	Req.	

Table 5-2: The CoDR compliance matrix from the Concept Design Proposal